

Quantitative Tract Integrity Profiles (Q-TIPs): A Novel Neuroimaging
Toolbox for Assessing Tract-based White Matter Integrity

by

Sohail Younas

A Thesis submitted to the Faculty of Graduate Studies of
The University of Manitoba
in partial fulfillment of the requirements of the degree of

MASTER OF SCIENCE

Biomedical Engineering

University of Manitoba

Winnipeg, MB, Canada

Copyright © 2017 by Sohail Younas

Abstract

Quantitative neuroimaging techniques for characterizing brain and spinal cord white matter typically rely on one of two common approaches: i) region-of-interest (ROI) or ii) voxel-wise analyses. Each of these approaches has particular benefits and drawbacks. ROI analyses extract data from relatively large, pre-determined regions, thereby facilitating the investigation of global white matter differences at the expense of sensitivity to small, localized changes. On the other hand, while voxel-wise analyses maintain high spatial resolution (i.e., by performing point-by-point analyses), sensitivity can suffer in-group analyses if, for example, lesion sizes/locations vary across subjects.

Alternatively, a few recent studies have proposed tract-based analyses that extract quantitative imaging values along white matter tracts. This has the advantage of studying large regions, while simultaneously preserving sensitivity to small, localized changes. However, although promising, existing tools for along-tract analyses have several fundamental limitations. Most importantly, they use complicated in-house software with command-line interfaces; they are platform dependent; and they rely on tractography to specify the orientation of each white matter tract, which therefore requires diffusion-imaging data to be acquired and extensively processed.

In this thesis, I have sought to address these issues by developing a toolbox called “Quantitative Tract Integrity Profiles (Q-TIPs)” that: is purely MATLAB-based (making it compatible with most operating systems), has a flexible and user-friendly interface, and will be distributed as a standalone toolbox for the popular Statistical Parametric Mapping (SPM) software package. This toolbox extracts the orientation of any ROI mask by

calculating the medial axis using Voronoi and Delaunay algorithms, and then cross-sectional segments along the extracted medial axis are used to create profiles based on any quantitative white matter magnetic resonance imaging metric (e.g., diffusion tensor imaging, myelin water imaging, magnetization transfer imaging, etc.). As a result, this toolbox will enable future neuroimaging studies to more easily and flexibly quantify white matter imaging signals along individual tracts as a function of neural development, healthy aging, traumatic brain injury, or neurodegenerative disease.

Acknowledgements

I would like to express my special appreciation and thanks to my advisor Dr. CHASE FIGLEY, you have been a tremendous mentor for me. I would like to thank you for encouraging my research and for allowing me to grow as a researcher. Your advice on both research as well as on my career have been priceless.

I would also like to thank my committee members (Dr. MELANIE MARTIN, Dr. JENNIFER KORNELSEN, Dr. SHERIF SHERIF and Dr. YANG WANG) for their input and guidance.

I would like to acknowledge financial support from two scholarships (the University of Manitoba Graduate Fellowship and Manitoba Graduate Fellowship) and operating grants from the Natural Sciences and Engineering Research Council and Brain Canada Foundation for supporting my project.

I am grateful to Dr. NASIR UDDIN, TERESA FIGLEY, ANWAR SHATIL and KEVIN SOLAR for continuously providing suggestions/recommendations during the project.

Last but not least, a special thanks to my family. Words cannot express how grateful I am to my mother, my father and my siblings for all of the sacrifices that you've made on my behalf. Your prayers for me were what sustained me thus far.

At the end, I would like to express appreciation to my all my loved ones who have been secretly praying for my success ☺

Thesis Format

The following document has been prepared as a manuscript-style (sandwich) thesis in accordance with the University of Manitoba's Faculty of Graduate Studies Thesis Guidelines. Chapter 1 is intended to provide a general background of the concepts and terminology used throughout the remainder of the thesis, and outlines the primary motivations and objectives. Chapter 2 and Chapter 3 have been prepared in manuscript format, and describe different components of the overarching research contributions. Finally, Chapter 4 provides a general conclusion and discusses future directions.

Table of Contents

ACKNOWLEDGEMENTS.....	IV
THESIS FORMAT.....	V
LIST OF FIGURES	X
LIST OF TABLES	XIII
CHAPTER 1	
GENERAL INTRODUCTION	1
1.1 INTRODUCTION	1
1.2 WHAT IS MRI?	2
1.3 MRI IN DETECTION OF MULTIPLE SCLEROSIS WHITE MATTER.....	3
1.4 MR IMAGING TECHNIQUES.....	4
1.4.1 <i>Diffusion Tensor Imaging (DTI)</i>	5
1.4.2 <i>Magnetization Transfer Imaging (MTI)</i>	5
1.4.3 <i>Myelin Water Imaging (MWI)</i>	6
1.5 MRI ANALYSIS TECHNIQUES	6
1.5.1 <i>Qualitative Analysis</i>	6
1.5.2 <i>Quantitative Analysis</i>	7
1.5.2.1 Region-of-Interest (ROI) Analyses	7
1.5.2.2 Voxel-Wise Analyses.....	8
1.5.2.3 Tract-Based (or Along-Tract) Analyses.....	10

1.6	MOTIVATION AND OBJECTIVES.....	14
1.6.1	<i>Objective</i>	15
1.7	REFERENCES.....	16

CHAPTER 2

DEVELOPMENT, IMPLEMENTATION, AND VALIDATION OF A MEDIAL

AXIS EXTRACTION ALGORITHM FOR COMPLEX 3D OBJECTS 26

	ABSTRACT.....	26
2.1	INTRODUCTION.....	27
2.2	PRELIMINARY DESCRIPTION OF VORONOI DIAGRAMS.....	30
2.3	2-D METHODOLOGY DESCRIPTION OF VORONOI DIAGRAMS.....	32
2.3.1	<i>Voronoi Diagram of a 2D Image</i>	32
2.3.2	<i>Initial cleaning of the Raw Voronoi Skeleton</i>	32
2.3.3	<i>Pruning the Raw Voronoi Skeleton</i>	32
2.3.4	<i>Summary</i>	36
2.4	INTERPOLATION.....	37
2.4.1	<i>Nearest Neighbors Search Algorithm</i>	37
2.5	3-D METHODOLOGY.....	41
2.6	RESULT.....	42
2.6.1	<i>Experiment 1</i>	43
2.6.2	<i>Experiment 2</i>	44
2.6.3	<i>Experiment 3</i>	46
2.7	DISCUSSION.....	50
2.8	CONCLUSION.....	51

2.9 REFERENCES	52
 CHAPTER 3	
QUANTITATIVE TRACT INTEGRITY PROFILES (Q-TIPS)	
A NOVEL MATLAB TOOLBOX FOR ASSESSING WHITE MATTER	
INTEGRITY	58
ABSTRACT	58
3.1 INTRODUCTION	59
3.2 OBJECTIVE	60
3.3 METHODOLOGY	61
3.3.1 <i>Dilation</i>	62
3.3.2 <i>Medial Axis Extraction</i>	64
3.3.3 <i>Noise Removal/Smoothing of Medial Axis</i>	64
3.3.4 <i>Path-Finding Algorithm</i>	65
3.3.5 <i>Cross-Sectional Slicing</i>	67
3.4 FUNCTIONAL FLOWCHART FOR Q-TIPS	69
3.5 RESULTS	71
3.6 DISCUSSION	76
3.7 CONCLUSION	77
3.8 REFERENCES	78
 CHAPTER 4	
GENERAL DISCUSSION AND CONCLUSION	82
4.1 FUTURE DEVELOPMENTS	83

4.1.1 *Graphical User Interface (GUI)* 84

4.1.2 *Optimizing Processing Time* 84

4.1.3 *Validation and Quantification of Tract Profiles* 84

4.1.4 *Releasing the Toolbox* 85

APPENDIX A

LIST OF ACRONYMS 86

APPENDIX B 88

List of Figures

<i>Figure 1-1: Example of an ROI analysis of FA in various sub-regions of the corpus callosum..</i>	8
<i>Figure 1-2: An Example of Tract-Based Spatial Statistics (TBSS), which is an approach for voxel-wise, white matter analyses..</i>	10
<i>Figure 1-3: Example of tract-based analysis..</i>	11
<i>Figure 1-4: Sampling of streamlines using the B-spline cubic algorithm.</i>	12
<i>Figure 1-5: Flow diagram of Automatic Fiber Quantification (AFQ)..</i>	13
<i>Figure 1-6: An example of the fronto-occipital fasciculus fractional anisotropy profile..</i>	14
<i>Figure 2-1: Main pipeline for different skeletonization algorithms.</i>	30
<i>Figure 2-2: (a) Division of space between two points. (b) Voronoi diagram of n sites and its main components.</i>	31
<i>Figure 2-3: Demonstration of the Pruning Process.</i>	35
<i>Figure 2-4: Refined skeleton after pruning process.</i>	36
<i>Figure 2-5: Block diagram of the 2D skeletonization procedure using a Voronoi diagram and pruning algorithm.</i>	37
<i>Figure 2-6: Delaunay triangles for n points.</i>	39
<i>Figure 2-7: Demonstration of the nearest neighbor search algorithm with respect to point P_1.</i>	40

<i>Figure 2-8: Demonstration of the nearest neighbor search algorithm with respect to point P_2.</i>	40
<i>Figure 2-9: Final result of the nearest neighbor algorithm.</i>	41
<i>Figure 2-10: 3D medial axis extraction flow chart.</i>	42
<i>Figure 2-11: Effect of T on the medial axis pruning (a) at $\pi/3$ (b) at $\pi/2$ (c) at $2\pi/3$ (d) at π (e) at 2π.</i>	43
<i>Figure 2-12: Results of 2D Voronoi Algorithms tested on five randomly selected images from the MPEG-7 database.</i>	44
<i>Figure 2-13: All four outputs from our 3D Medial Axis Algorithm.</i>	45
<i>Figure 2-14: Typical results of our 3D Medial Axis Algorithm on other smooth, continuous 3D images.</i>	46
<i>Figure 2-15: All four outputs from the 3D medial axis extraction algorithm.</i>	47
<i>Figure 2-16: An example in which the 3D Voronoi algorithm failed to produce an accurate medial axis (since all four of the outputs contain either erroneous points or holes).</i>	48
<i>Figure 2-17: The resulting 3D skeleton after the interpolation algorithm was applied to the XYZ-common intersection.</i>	48
<i>Figure 2-18: Testing results from other white matter atlases.</i>	49
<i>Figure 3-1: Image processing pipeline of Q-TIPs.</i>	62
<i>Figure 3-2: Effect of dilation using 3x3 structure element. It can see that gap between two objects can be reduced using dilation method.</i>	63
<i>Figure 3-3: Dilation process in Q-TIPs.</i>	63
<i>Figure 3-4: Improper dilation results</i>	64

<i>Figure 3-5: Noise Removal Algorithm.....</i>	<i>65</i>
<i>Figure 3-6: Complex features of medial axes.....</i>	<i>66</i>
<i>Figure 3-7: Feature labeling (branches and bifurcations).</i>	<i>66</i>
<i>Figure 3-8: Results of path-finding algorithm.....</i>	<i>67</i>
<i>Figure 3-9: Perpendicular direction at P_1.....</i>	<i>68</i>
<i>Figure 3-10: Slicing performed at P_1 and masking with the cross-section of the original (undilated) ROI.....</i>	<i>69</i>
<i>Figure 3-11: Functional flowchart of Q-TIPs.....</i>	<i>70</i>
<i>Figure 3-12: Outputs at different stages of Q-TIPs for a representative white matter ROI mask (from an existing atlas).....</i>	<i>71</i>
<i>Figure 3-13: Outputs at different stages of Q-TIPs for a different white matter ROI mask (from an existing atlas).....</i>	<i>72</i>
<i>Figure 3-14: Outputs at different stages of Q-TIPs for a multi-ends white matter ROI mask (from an existing atlas).....</i>	<i>73</i>
<i>Figure 3-15: Tract-profiles (fractional anisotropy, mean diffusivity profile, myelin water fraction, and T1w/T2w ratio) are generated using Q-TIPs.....</i>	<i>74</i>
<i>Figure 3-16: Tract-profiles (fractional anisotropy, mean diffusivity profile, myelin water fraction, and T1w/T2w ratio) are generated using Q-TIPs.....</i>	<i>75</i>
<i>Figure 3-17: Example of the wrong cross-sectional slice at bends. (b) Red and green circles indicate results of wrong cross-sectional slicing.....</i>	<i>77</i>

List of Tables

Table 2-1: Processing time for Smooth and Continuous Database..... 50

Table 2-2: Processing time for White Matter Atlases..... 51

Chapter 1

General Introduction

1.1 Introduction

The brain is arguably the most interesting and the least understood organ in the human body. For hundreds of years, researchers have been trying to understand the relationships between the brain and perceptual, cognitive, emotional and behavioural processes [1]. However, as research progressed, scientists began associating different regions of the brain with specific functions: first by studying patients with injuries to particular sub-regions [2, 3], then by stimulating different parts of the cortex using electricity to evoke responses [4], and later by recording small electrical signals elicited during specific tasks [5, 6].

Furthermore, as medical imaging technology advanced, the structural and functional picture of the brain started becoming clearer [7]. With the introduction of x-ray computed tomography (CT) during the 1970s, clinicians were finally able to identify features and pathologies inside the brain without exploratory surgery [8, 9]. Later, positron emission tomography (PET), a nuclear medicine imaging technique was

developed. PET measures different essential body functions (such as blood flow, oxygen use, and glucose consumption) during execution of simple cognitive tasks so that the physiology and anatomy maps of the organ can be created [10, 11, 12, 13]. Magnetic resonance imaging (MRI) is a non-invasive and versatile medical imaging technology for studying the central nervous system (CNS) due to its broad spectrum of contrast mechanisms [14], which provide excellent soft tissue distinction. With the invention of new MRI techniques, different research fields emerged. For example, in the early 1990s, blood oxygenation level–dependent (BOLD) imaging was first used to study increased neuronal activity in the brain [15]. This method captured the attention of hundreds of investigators and, due to its ability to detect brain function and explore the mind, was called functional magnetic resonance imaging (fMRI) [16, 17].

1.2 What is MRI?

MRI is a diagnostic test that uses magnetic fields to create images of the human body without the use of ionizing radiation [18]. Depending on operator-defined parameters, scans can be performed with different fields of view, spatial resolutions, and tissue contrasts; and, because of this flexibility, it can be used to diagnose a broad range of diseases. However, in addition to clinical applications, researchers also use MRIs to study structural details and functional behavior of the brain.

MRI, based on the principle of nuclear magnetic resonance (NMR), exploits the magnetic properties of certain atomic nuclei – usually hydrogen protons from water molecules – in biological tissues [19]. These nuclei spin creating a small magnetic field,

so when a strong magnetic field is introduced (as is the case in an MRI machine), most of the nuclei align with that field [20]. A radio frequency magnetic field is then applied to disrupt the nuclei (via electromagnetic induction), which simultaneously imparts phase coherence and forces some of them to into a higher energy state, producing non-zero (typically 90-degree or 180-degree) net transverse magnetization relative to the static magnetic field. Since the radio frequency pulse added energy to the system and forced the nuclei out of their low-energy states, these nuclei will then realign with the static magnetic field and lose their phase coherence once the pulse is turned off. However, in the brief period following the radio frequency pulse, MRI can detect the amount of transverse magnetization in different locations, and these signals can be used to produce detailed images with the amount of contrast depending on various scan parameters and how quickly the nuclei in various tissues lose their net transverse magnetization.

1.3 MRI in detection of Multiple Sclerosis White Matter

Multiple Sclerosis (MS) is a disease that affects the central nervous system (CNS), which consists of the brain, spinal cord, and optic nerves. Everything the human body does (e.g. walking, solving a problem, or simply breathing, etc.) relies on the proper functioning of the CNS. The human brain and spinal cord are made up of billions of nerve cells (neurons), which continuously send and receive signals to communicate with each other to perform tasks. For the majority of these neurons, the axons (i.e., extensions used for transmitting signals from the cell body) are covered by a myelin sheath, which is a fatty, white substance that is made of oligodendrocytes and helps neural signals to be effectively and efficiently communicated. Because of the white appearance, brain regions

containing myelinated axons are commonly referred to as ‘white matter’ regions. However, in the case of MS, the body’s immune system (that normally protects against foreign substances such as bacteria and viruses) attacks the myelin sheath, and with the passage of time, it destroys the myelin and disrupts the communication between neurons. The symptoms (either temporary or permanent) of MS are different from one individual to another, but some of the most common effects early in the disease include visual problems and numbness, tingling and/or weakness in the arms, hands, legs or feet; and, these often progress to blindness and/or paralysis later in the disease.

MS is diagnosed by a combination of medical history, brain imaging with MRI, and other tests [21, 22]. On MRI scans of the brain and spinal cord, the damaged areas of myelin (called lesions) appear as abnormally dark or light spots – most commonly observed within white matter regions (although research has more recently started to focus on ‘gray matter’ lesions as well). Moreover, in addition to conventional MRI contrasts, research has also started to focus on more advanced MRI techniques: some of which are briefly discussed below.

1.4 MR Imaging Techniques

The goal of the following section is to briefly outline a few of the advanced quantitative imaging techniques that have been applied to white matter.

1.4.1 Diffusion Tensor Imaging (DTI)

DTI reveals the microstructure and anatomy of biological tissues by measuring the diffusion of the water molecules within each voxel [23, 24, 25]. DTI-based quantitative metrics include fractional anisotropy and mean diffusivity. Fractional anisotropy (FA) is a measure of the directionality of diffusion and ranges from 0 to 1 [26]. The value 0 represents isotropic diffusion (unrestricted or equally restricted in all directions), and the value 1 represents diffusion only along one axis (entirely restricted along all other orientations). Mean diffusivity (MD) is a scalar value that defines the average diffusion across directions (i.e., the average amount of water movement within each voxel) [25]. High FA and small MD are therefore thought to reflect greater microstructural integrity and more parallel axonal packing. Conversely, in patients with white matter damage, FA values would be expected to decrease and MD values would be expected to increase compared to healthy subjects [27].

1.4.2 Magnetization Transfer Imaging (MTI)

MTI relies on the principle of magnetization transfer (i.e., the transfer of nuclear spin polarization and coherence from one population of nuclei to another) in order to infer information about hydrogen nuclei bound within macromolecules and/or membranes (e.g., myelin), which are otherwise invisible using conventional MRI [28]. MTI allows the magnetic transfer ratio (MTR) to be computed as $MTR = (S_o - S_{MT})/S_o$, where S_o and S_{MT} are the magnitudes of the tissue signals before and after MT pulses have been applied, respectively. Usually, white matter has

higher MTR values than gray matter due to higher membrane densities and the presence of myelin; and significantly reduced MTR in white matter regions is typically thought to indicate the presence inflammation or white matter damage [29].

1.4.3 Myelin Water Imaging (MWI)

Multicomponent T2-relaxation MWI measures the rate at which transverse magnetization is lost in each region, and then uses this information to separate the signal into different water components (i.e., fast, medium, and slow), where the fast component represents the signal from water molecules trapped within the myelin [30]. The myelin water fraction (MWF), calculated by dividing the fast component by the sum of all three components, is therefore thought to reflect the degree of myelination within each region. This method has been validated using histological methods [31], and decreased MWFs have been measured in MS subjects, compared with healthy controls [32].

1.5 MRI Analysis Techniques

In the literature, different qualitative and quantitative techniques have been implemented to assess white matter integrity using MRI.

1.5.1 Qualitative Analysis

Fiber tracking (or “tractography”) is a qualitative method that estimates and visually represents white matter fibers/tracts based on the principal orientations of water

diffusion in white matter [33, 34, 35, 36]. These diffusion-based white matter reconstructions are typically called “streamlines”, and are able to provide subject-specific 3D maps of white matter pathways in both healthy and clinical populations [37, 38]. For example, corticospinal tract connectivity can be visualized using tractography, and can be used to show differences between stroke patients and healthy subjects [39, 40]. However, although this technique provides visually appealing displays of white matter, it is not inherently quantitative, and even semi-quantitative measures (such as the number of streamlines [41]) are entirely dependent on input parameters and the diffusion model that is selected.

1.5.2 Quantitative Analysis

On the other hand, quantitative approaches for DTI and other advanced white matter imaging methods have typically fallen into one of two categories: region-of-interest (ROI) or voxel-wise analyses.

1.5.2.1 Region-of-Interest (ROI) Analyses

Specific regions of interest within the brain are extracted, and analyses are performed on those areas to draw conclusions in group studies [42]. ROIs can be defined either regarding structural or functional features [43]. Structural ROIs, in turn, can be defined either based on cytoarchitectonic features [44] or according to anatomical landmarks [45]. While, on the other hand, functional ROIs are defined based on the

analysis of functional data [46, 47]. One standard approach for extracting these functional ROIs is placing a small sphere around the local maxima in the statistical map [43, 48].

ROI analyses require a predefined functional hypothesis related to a particular anatomically distinct region of the brain. For example, this method would be appropriate if one wanted to determine the effect of age on microstructural integrity within different areas of the corpus callosum [49, 50], and to draw conclusions about how fractional anisotropy (FA) values in the various regions of the corpus callosum are affected by age shown in Figure 1-1. However, while this approach successfully facilitates the investigation of global or distributed white matter changes in a group or between-subject analyses, the sensitivity is reduced for small, localized changes that are common in multiple sclerosis and many other white matter disorders.

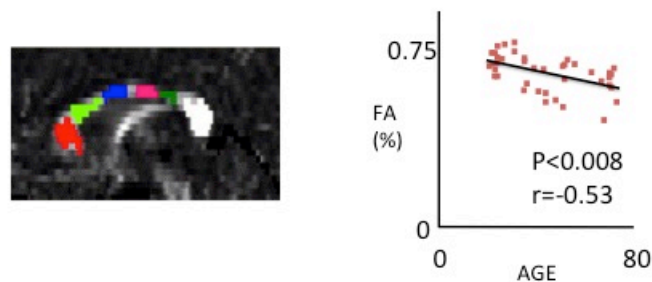


Figure 1-1: Example of an ROI analysis of FA in various sub-regions of the corpus callosum. The decline of FA showed a significant negative correlation with age in the corpus callosum. Reproduced with permission from Ota et al. [49] (See Appendix B).

1.5.2.2 Voxel-Wise Analyses

Voxel-wise analyses calculate MR metrics for each voxel within the brain, and then, perform point-by-point analyses across subjects as shown in Figure 1-2. The subjects are first co-registered, and then comparisons are carried out for group-wise

differences in each co-registered voxel [51]. It is highly dependent on the normalization or registration step within the pre-processing pipeline. Image registration is the process of aligning the geometry (size and shape), and topology of different brains – taken at different times, from different viewpoints, and/or by different sensors [52]. Examples of various types of registration are:

1. Pairwise Registration:

Includes nonlinear registration using basis functions [53], Unified segmentation [54], Hierarchical Attribute Matching Mechanism for Elastic Registration (HAMMER) [55].

2. Groupwise registration:

Includes Implicit reference-based group-wise image registration (IRG) [56], Diffeomorphic Anatomical Registration using Exponentiated Lie Algebra (DARTEL) [57].

Although this approach has the advantage of having high spatial resolution (and potentially better sensitivity to small, localized changes), proper registration of inter-subject data is vital for voxel-based methods since misalignments of corresponding anatomical regions may result in an increased number of false-negative or false-positive voxels and thus affect the overall sensitivity [58, 59, 60, 61]. Also, the voxel-wise analysis does not work well if changes are not spatially conserved across the study population (e.g., if each patient has white matter lesions in different locations).

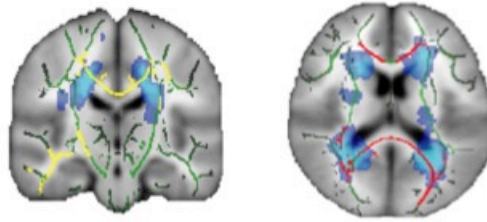


Figure 1-2: An Example of Tract-Based Spatial Statistics (TBSS), which is an approach for voxel-wise, white matter analyses. Yellow shows where FA correlates negatively with EDSS disability score. Red shows negative correlation with lesion volume. Blue shows the group mean lesion distribution. Green shows mean FA skeleton. Reproduced with permission from Smith et al. [60] (See Appendix B).

1.5.2.3 Tract-Based (or Along-Tract) Analyses

A small number of recent studies [41, 62, 63] have proposed tract-based analysis approaches to extract white matter values along tract (i.e., to construct white matter curves or profiles along specific white matter pathways) as demonstrated in Figure 1-2. These studies have plotted diffusion imaging measures of healthy subjects to show their tract profiles. This approach has the advantage of studying large regions while maintaining sensitivity to small, localized changes.

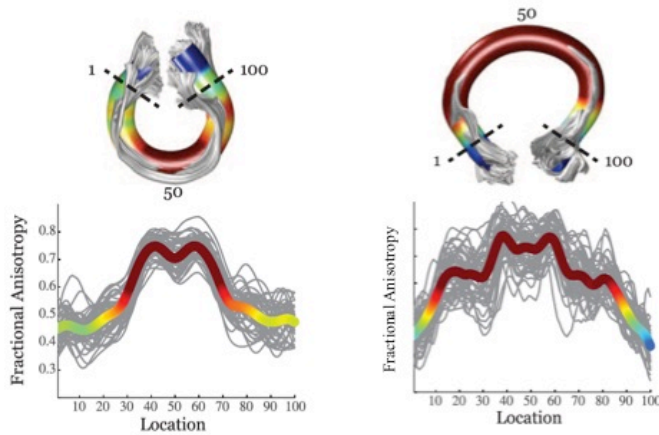


Figure 1-3: Example of tract-based analysis. Can clearly see if white matter integrity changes along the length of the tract. Reproduced with permission from Yeatman et al. [63] (See Appendix B).

A brief summary of general end-to-end workflow for the along-tract analysis described by Colby et al. [41] is as follows: First, TrackVis (<http://www.trackvis.org>) extracts the exact positions of tract groups for each subject by fitting diffusion tensor models to raw data. From the tract groups' information, collections of streamlines are generated using a brute force tractography algorithm (e.g. Fiber Assignment by Continuous Tracking (FACT) [33]), that represent white matter pathways across the entire brain. After this, streamlines reorientation is done so that they all “start” at the same end. These reoriented streamlines are then sampled using cubic B-splines as shown in Figure 1-3, and the underlying scalar volume (e.g. fractional anisotropy map) is obtained for the new set of resampled streamlines. And finally, performing cross-sectional statistical methods along the particular tract of each subject creates tract profiles.

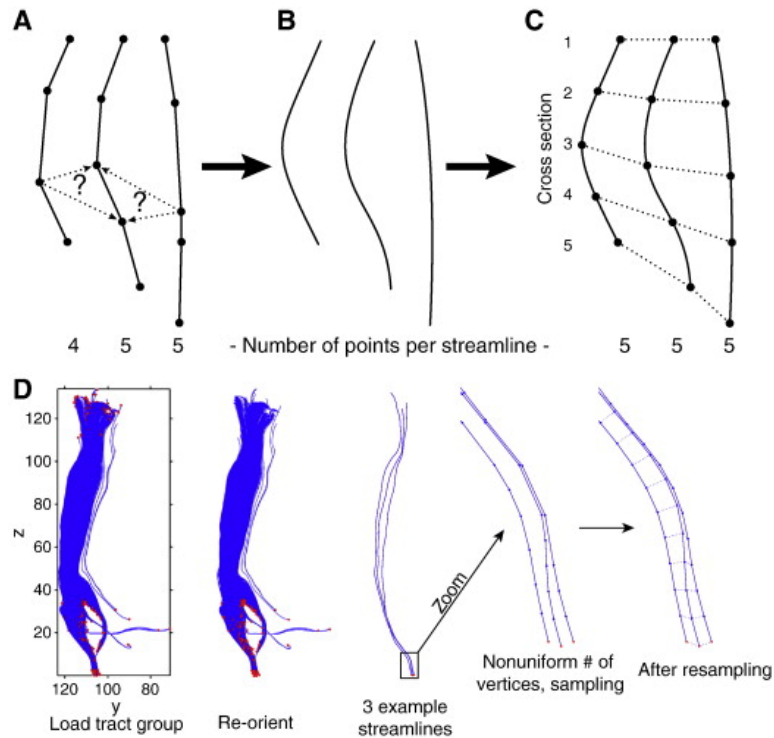


Figure 1-4: Sampling of streamlines using the B-spline cubic algorithm. Reproduced with permission from Colby et al. [41] (See Appendix B).

Yeatman et al. (2012) developed open-source “Automated Fiber Quantification (AFQ)” software for creating tract profiles of cerebral white matter pathways [63]. AFQ performs whole-brain fiber tracking using deterministic streamlines tracking algorithm (STA) [64]. Then, fiber segmentation is performed, in which, fibers are assigned to a particular group using a waypoint ROI procedure [65], followed by fiber tract refinements. Each candidate fiber is compared with that of fiber tract probability maps, created by Hua et al. [66] and, cleaning and clipping are performed to remove unwanted

fibers from the fiber bundle. Each fiber in a particular fiber bundle is resampled to 100 equally spaced nodes, and diffusion properties are calculated cross-sectionally at each node to create tract profiles. A flow diagram of AFQ is shown in Figure 1-4.

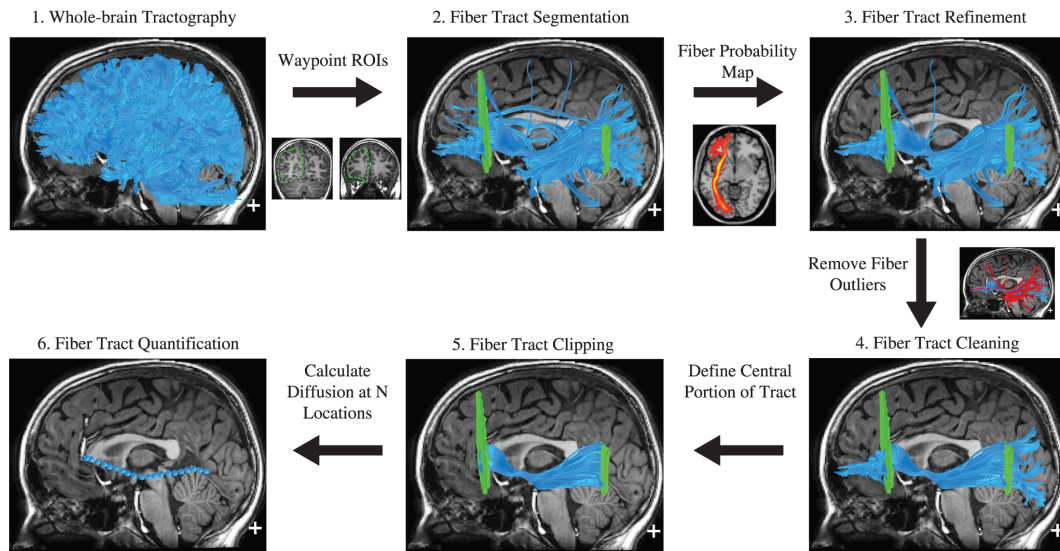


Figure 1-5: Flow diagram of Automatic Fiber Quantification (AFQ). Whole-brain tractography is performed, followed by ROI extraction using probability map. After ROI extraction, refinement, cleaning, and clipping are done. Finally, tract profile is created. With permission taken from Yeatman et al. [63] (See Appendix B).

Walsh et al. also reported along-tract analysis based on tractography [62]. They first performed motion-correction on the data using CATNAP (Coregistration, Adjustment, and Tensor-solving: a Nicely Automated Program) [67] and then performed whole brain deterministic tractography using DTI Studio [68] with liberal parameters ($FA > 0.13$ & turning angle $< 45^\circ$). Finally, they showed tract-profiles of MS patients having large amounts of damage to fronto-occipital fasciculus as compared to those with a minimal amount of damage as shown in Figure 1-5.

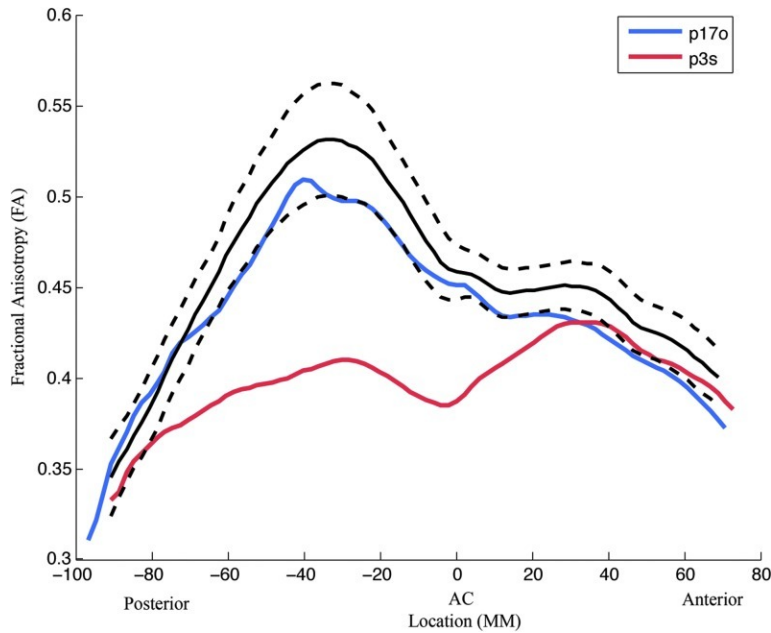


Figure 1-6: An example of the fronto-occipital fasciculus fractional anisotropy profile. Solid and dotted black curves show healthy subjects curve with standard deviation respectively. The red curve represents MS patient having a significant amount of damage when compared with those having minimal damage. Reproduced with permission from Walsh et al. [62] (See Appendix B).

1.6 Motivation and Objectives

Although promising, each of the aforementioned tract-based approaches has several fundamental limitations, most importantly:

- 1) They are platform-dependent (i.e., they all rely on the Linux platform and cannot be run on Windows-based workstations).
- 2) They use complicated, in-house software that requires multiple steps and command line inputs.

- 3) They are exclusively for DTI data (i.e., because they rely on tractography streamlines to determine where/how to extract the data to generate the quantitative curves) and thus require a significant amount of data pre-processing and are not generalizable to other quantitative white matter imaging methods such as magnetization transfer imaging (MTI), multi-component T2-relaxation myelin water imaging (MWI), etc.
- 4) For quantitative analysis, they rely primarily on subjective (i.e., visual) examination of these curves, and are therefore still only semi-quantitative.

1.6.1 Objective

To address the issues present in recent studies [41, 62, 63], in this thesis, I have developed a toolbox for assessing the integrity of white matter tracts called “Quantitative Tract Integrity Profiles (Q-TIPs).” Q-TIPs offers the following features:

Feature 1: Cross-Platform Capability

Whereas other along-tract analysis software packages are exclusively Linux-based, our toolbox works on multiple platforms. Our analysis software has been developed entirely in MATLAB, which is available to most neuroimaging researchers, and can run on most of the common operating systems (e.g. Windows, Mac, Linux).

Feature 2: User-Friendly and Standalone

Existing tract-based analysis packages use sophisticated in-house software that requires scripting and/or command line. Our toolbox will be distributed as a standalone

toolbox for the popular Statistical Parametric Mapping (SPM) software package, which is a set of free MATLAB-based programs for image processing and statistical analyses related to structural and functional neuroimaging experiments. Also, a Graphical User Interface (GUI) will be provided to operate this toolbox easily, as graphical icons and visual indicators are much more comfortable than text-based interfaces.

Feature 3: Generalizable Across MRI Modalities

Another limitation of recent approaches is that they all require, and are exclusively for use with diffusion tensor imaging data. Tractography is performed to extract lines along the tract. Once the lines are obtained, then retrieving values along the lines is a relatively simple task. However, if a researcher has not performed tractography, these recently existing methods will not work.

In order to handle this complication, our toolbox extracts the medial axis along with skeleton details of any 3D binary mask (i.e., atlas). This allows researchers to obtain any quantitative values (including MTR, MWF, FA, MD, etc.) from the cross-section of the atlas while moving along the medial axis of the atlas and reorienting the sampling plane accordingly.

1.7 References

- [1] A. D. Wagner and J. D. . Gabrieli, “On the relationship between recognition familiarity and perceptual fluency: Evidence for distinct mnemonic processes,” *Acta Psychol. (Amst)*., vol. 98, no. 2–3, pp. 211–230, 1998.
- [2] H. Damasio, T. Grabowski, R. Frank, A. M. Galaburda, and A. R. Damasio, “The

- return of Phineas Gage: Clues about the brain from the skull of a famous patient,” *Science*, vol. 264, no. 5162. pp. 1102–1105, 1994.
- [3] I. T. Draper, *the Working Brain (an Introduction To Neuropsychology)*, vol. 37, no. 3. 1974.
- [4] S. Borchers, M. Himmelbach, N. Logothetis, and H.-O. Karnath, “Direct electrical stimulation of human cortex - the gold standard for mapping brain functions?,” *Nat. Rev. Neurosci.*, vol. 13, no. 1, pp. 63–70, 2012.
- [5] P. H. Schiller and M. Stryker, “Single-unit recording and stimulation in superior colliculus of the alert rhesus monkey.,” *J. Neurophysiol.*, vol. 35, no. 6, pp. 915–924, 1972.
- [6] A. B. Vallbo, K. E. Hagbarth, H. E. Torebjork, and B. G. Wallin, “Somatosensory, proprioceptive, and sympathetic activity in human peripheral nerves,” *Physiol. Rev.*, vol. 59, no. 4, pp. 919–957, 1979.
- [7] W. R. Hendee, M. J. Welch, N. R. Dunnick, L. B. Bresolin, R. L. Arenson, S. Baum, and J. H. Thrall, “Blueprint for Imaging in Biomedical Research,” *Radiology*, vol. 244, no. 1, 2007.
- [8] J.-L. Sablayrolles, N. Al Attar, and P. Nataf, “New trends in non-invasive coronary angiography with multislice CT,” *Surg. Technol. Int.*, vol. 13, pp. 205–213, 2004.
- [9] J. Ueno, T. Murase, K. Yoneda, T. Tsujikawa, S. Sakiyama, and K. Kondoh, “Three-dimensional imaging of thoracic diseases with multi-detector row CT.,” *J. Med. Invest.*, vol. 51, no. 3–4, pp. 163–170, 2004.
- [10] S. T. Witt, A. R. Laird, and M. E. Meyerand, “Functional neuroimaging correlates of finger-tapping task variations : An ALE meta-analysis,” vol. 42, pp. 343–356,

2008.

- [11] R. Loose, K. Lutz, K. Specht, N. J. Shah, and L. Jancke, “Cortical activations during paced finger-tapping applying visual and auditory pacing stimuli,” vol. 10, pp. 51–66, 2000.
- [12] V. Gountouna, D. E. Job, A. M. McIntosh, T. W. J. Moorhead, G. K. L. Lymer, H. C. Whalley, J. Hall, G. D. Waiter, D. Brennan, D. J. Mcgonigle, T. S. Ahearn, J. Cavanagh, B. Condon, D. M. Hadley, I. Marshall, A. D. Murray, J. D. Steele, J. M. Wardlaw, and S. M. Lawrie, “NeuroImage Functional Magnetic Resonance Imaging (fMRI) reproducibility and variance components across visits and scanning sites with a finger tapping task,” *Neuroimage*, vol. 49, no. 1, pp. 552–560, 2010.
- [13] B. Pollok, J. Gross, and A. Schnitzler, “How the brain controls repetitive finger movements,” vol. 99, pp. 8–13, 2006.
- [14] A. L. Alexander, J. E. Lee, M. Lazar, and A. S. Field, “Diffusion Tensor Imaging of the Brain,” vol. 4, no. July, pp. 316–329, 2007.
- [15] S. Ogawa, T. M. Lee, A. R. Kay, and D. W. Tank, “Brain magnetic resonance imaging with contrast dependent on blood oxygenation.,” *Proc. Natl. Acad. Sci. U. S. A.*, vol. 87, no. 24, pp. 9868–72, 1990.
- [16] K. K. Kwong, J. W. Belliveau, D. A. Chesler, I. E. Goldberg, R. M. Weisskoff, B. P. Poncelet, D. N. Kennedy, B. E. Hoppel, M. S. Cohen, and R. Turner, “Dynamic magnetic resonance imaging of human brain activity during primary sensory stimulation.,” *Proc. Natl. Acad. Sci. U. S. A.*, vol. 89, no. 12, pp. 5675–5679, 1992.
- [17] P. M. Matthews, G. D. Honey, and E. T. Bullmore, “Applications of fMRI in

- translational medicine and clinical practice.,” *Nat. Rev. Neurosci.*, vol. 7, no. 9, pp. 732–44, 2006.
- [18] T. W. Redpath, “Principles of nuclear magnetic resonance in one and two dimensions,” *Magn. Reson. Imaging*, vol. 6, no. 3, p. 349, 1988.
- [19] D. B. Plewes and W. Kucharczyk, “Physics of MRI: A primer,” *Journal of Magnetic Resonance Imaging*, vol. 35, no. 5, pp. 1038–1054, 2012.
- [20] W. R. Nitz, T. Balzer, D. S. Grosu, and T. Allkemper, “Principles of magnetic resonance,” in *Clinical MR Imaging (Third Edition): A Practical Approach*, 2010, pp. 1–105.
- [21] W. I. McDonald, A. Compston, G. Edan, D. Goodkin, H. P. Hartung, F. D. Lublin, H. F. McFarland, D. W. Paty, C. H. Polman, S. C. Reingold, M. Sandberg-Wollheim, W. Sibley, A. Thompson, S. Van Den Noort, B. Y. Weinschenker, and J. S. Wolinsky, “Recommended diagnostic criteria for multiple sclerosis,” *Ann. Neurol.*, vol. 50, pp. 121–127, 2001.
- [22] C. H. Polman, S. C. Reingold, G. Edan, M. Filippi, H. P. Hartung, L. Kappos, F. D. Lublin, L. M. Metz, H. F. McFarland, P. W. O’Connor, M. Sandberg-Wollheim, A. J. Thompson, B. G. Weinschenker, and J. S. Wolinsky, “Diagnostic criteria for multiple sclerosis: 2005 Revisions to the ‘McDonald Criteria,’” *Annals of Neurology*, vol. 58, no. 6, pp. 840–846, 2005.
- [23] L. J. O’Donnell and C. F. Westin, “An introduction to diffusion tensor image analysis,” *Neurosurgery Clinics of North America*, vol. 22, no. 2, pp. 185–196, 2011.
- [24] P. J. Basser, J. Mattiello, and D. LeBihan, “MR diffusion tensor spectroscopy and

- imaging.,” *Biophys. J.*, vol. 66, no. 1, pp. 259–67, 1994.
- [25] D. Le Bihan, J. F. Mangin, C. Poupon, C. a Clark, S. Pappata, N. Molko, and H. Chabriat, “Diffusion tensor imaging: concepts and applications.,” *J. Magn. Reson. Imaging*, vol. 13, no. 4, pp. 534–546, 2001.
- [26] P. J. Basser and C. Pierpaoli, “Microstructural and physiological features of tissues elucidated by quantitative-diffusion-tensor MRI. 1996.,” *J. Magn. Reson.*, vol. 213, no. 2, pp. 560–70, 2011.
- [27] M. Inglese and M. Bester, “Diffusion imaging in multiple sclerosis: Research and clinical implications,” *NMR in Biomedicine*, vol. 23, no. 7. pp. 865–872, 2010.
- [28] R. I. Grossman, J. M. Gomori, K. N. Ramer, F. J. Lexa, and M. D. Schnall, “Magnetization transfer: theory and clinical applications in neuroradiology.,” *Radiographics*, vol. 14, no. 2, pp. 279–290, 1994.
- [29] Y. Ge, “Multiple sclerosis: The role of MR imaging,” *American Journal of Neuroradiology*, vol. 27, no. 6. pp. 1165–1176, 2006.
- [30] E. Alonso-Ortiz, I. R. Levesque, and G. B. Pike, “MRI-based myelin water imaging: A technical review,” *Magn. Reson. Med.*, vol. 73, no. 1, pp. 70–81, 2015.
- [31] C. Laule, I. M. Vavasour, G. R. W. Moore, J. Oger, D. K. B. Li, D. W. Paty, and A. L. MacKay, “Water content and myelin water fraction in multiple sclerosis: A T₂ relaxation study,” *J. Neurol.*, vol. 251, no. 3, pp. 284–293, 2004.
- [32] T. D. Faizy, C. Thaler, D. Kumar, J. Sedlacik, G. Broocks, M. Grosser, J. P. Stellmann, C. Heesen, J. Fiehler, and S. Siemonsen, “Heterogeneity of multiple sclerosis lesions in multislice myelin water imaging,” *PLoS One*, vol. 11, no. 3, 2016.

- [33] S. Mori, B. J. Crain, V. P. Chacko, and P. C. van Zijl, “Three-dimensional tracking of axonal projections in the brain by magnetic resonance imaging,” *Ann Neurol*, vol. 45, no. 2, pp. 265–269, 1999.
- [34] P. J. Basser, S. Pajevic, C. Pierpaoli, J. Duda, and A. Aldroubi, “In vivo fiber tractography using DT-MRI data,” *Magn. Reson. Med.*, vol. 44, no. 4, pp. 625–632, 2000.
- [35] J. C. Fernandez-Miranda, S. Pathak, J. Engh, K. Jarbo, T. Verstynen, F. C. Yeh, Y. Wang, A. Mintz, F. Boada, W. Schneider, and R. Friedlander, “High-definition fiber tractography of the human brain: Neuroanatomical validation and neurosurgical applications,” *Neurosurgery*, vol. 71, no. 2, pp. 430–453, 2012.
- [36] A. Romano, G. D’Andrea, G. Minniti, L. Mastronardi, L. Ferrante, L. M. Fantozzi, and A. Bozzao, “Pre-surgical planning and MR-tractography utility in brain tumour resection,” *Eur. Radiol.*, vol. 19, no. 12, pp. 2798–2808, 2009.
- [37] S. Farquharson, J.-D. Tournier, F. Calamante, G. Fabinyi, M. Schneider-Kolsky, G. D. Jackson, and A. Connelly, “White matter fiber tractography: why we need to move beyond DTI,” *J. Neurosurg.*, vol. 118, no. 6, pp. 1367–77, 2013.
- [38] J.-D. J. Tournier, S. Mori, and A. Leemans, “Diffusion tensor imaging and beyond,” *Magn. Reson. ...*, vol. 65, no. 6, pp. 1532–56, 2011.
- [39] G. Silasi and T. H. Murphy, “Stroke and the connectome: How connectivity guides therapeutic intervention,” *Neuron*, vol. 83, no. 6, pp. 1354–1368, 2014.
- [40] A. R. Carter, G. L. Shulman, and M. Corbetta, “Why use a connectivity-based approach to study stroke and recovery of function?,” *Neuroimage*, vol. 62, no. 4, pp. 2271–2280, 2012.

- [41] J. B. Colby, L. Soderberg, C. Lebel, I. D. Dinov, P. M. Thompson, and E. R. Sowell, "Along-tract statistics allow for enhanced tractography analysis," *Neuroimage*, vol. 59, no. 4, pp. 3227–3242, 2012.
- [42] A. Nieto-Castanon, S. S. Ghosh, J. A. Tourville, and F. H. Guenther, "Region of interest based analysis of functional imaging data," *Neuroimage*, vol. 19, no. 4, pp. 1303–1316, 2003.
- [43] R. A. Poldrack, "Region of interest analysis for fMRI," *Soc. Cogn. Affect. Neurosci.*, vol. 2, no. 1, pp. 67–70, 2007.
- [44] J. Rademacher, J. V. S. Caviness, H. Steinmetz, and A. M. Galaburda, "Topographical Variation of the Human Primary Cortices," *Cereb. Cortex*, vol. 3, no. August, pp. 313–329, 1993.
- [45] V. S. Caviness, J. Meyer, N. Makris, and D. N. Kennedy, "MRI-Based Topographic Parcellation of Human Neocortex: An Anatomically Specified Method with Estimate of Reliability," *J. Cogn. Neurosci.*, vol. 8, no. 6, pp. 566–587, 1996.
- [46] P. E. Turkeltaub, G. F. Eden, K. M. Jones, and T. a Zeffiro, "Meta-analysis of the functional neuroanatomy of single-word reading: method and validation.," *Neuroimage*, vol. 16, no. 3 Pt 1, pp. 765–780, 2002.
- [47] K. J. Friston, P. Rotshtein, J. J. Geng, P. Sterzer, and R. N. Henson, "A critique of functional localisers," *Neuroimage*, vol. 30, no. 4, pp. 1077–1087, 2006.
- [48] J. B. Julian, E. Fedorenko, J. Webster, and N. Kanwisher, "An algorithmic method for functionally defining regions of interest in the ventral visual pathway," *Neuroimage*, vol. 60, no. 4, pp. 2357–2364, 2012.

- [49] M. Ota, T. Obata, Y. Akine, H. Ito, H. Ikehira, T. Asada, and T. Suhara, “Age-related degeneration of corpus callosum measured with diffusion tensor imaging,” *Neuroimage*, vol. 31, no. 4, pp. 1445–1452, 2006.
- [50] D. H. Salat, D. S. Tuch, D. N. Greve, A. J. W. Van Der Kouwe, N. D. Hevelone, A. K. Zaleta, B. R. Rosen, B. Fischl, S. Corkin, H. Diana Rosas, and A. M. Dale, “Age-related alterations in white matter microstructure measured by diffusion tensor imaging,” *Neurobiol. Aging*, vol. 26, no. 8, pp. 1215–1227, 2005.
- [51] C. G. Schwarz, R. I. Reid, J. L. Gunter, M. L. Senjem, S. A. Przybelski, S. M. Zuk, J. L. Whitwell, P. Vemuri, K. A. Josephs, K. Kantarci, P. M. Thompson, R. C. Petersen, and C. R. Jack, “Improved DTI registration allows voxel-based analysis that outperforms Tract-Based Spatial Statistics,” *Neuroimage*, vol. 94, pp. 65–78, 2014.
- [52] B. Zitová and J. Flusser, “Image registration methods: A survey,” *Image Vis. Comput.*, vol. 21, no. 11, pp. 977–1000, 2003.
- [53] J. Ashburner and K. J. Friston, “Nonlinear spatial normalization using basis functions,” *Hum. Brain Mapp.*, vol. 7, no. 4, pp. 254–266, 1999.
- [54] J. Ashburner and K. J. Friston, “Unified segmentation,” *Neuroimage*, vol. 26, no. 3, pp. 839–851, 2005.
- [55] D. Shen and C. Davatzikos, “HAMMER: Hierarchical attribute matching mechanism for elastic registration,” *IEEE Trans. Med. Imaging*, vol. 21, no. 11, pp. 1421–1439, 2002.
- [56] X. Geng, G. E. Christensen, H. Gu, T. J. Ross, and Y. Yang, “Implicit reference-based group-wise image registration and its application to structural and functional

- MRI,” *Neuroimage*, vol. 47, no. 4, pp. 1341–1351, 2009.
- [57] J. Ashburner, “A fast diffeomorphic image registration algorithm,” *Neuroimage*, vol. 38, no. 1, pp. 95–113, 2007.
- [58] J. Ashburner and K. J. Friston, “Voxel-Based Morphometry—The Methods,” *Neuroimage*, vol. 11, no. 6, pp. 805–821, 2000.
- [59] F. L. Bookstein, “‘Voxel-Based Morphometry’ Should Not Be Used with Imperfectly Registered Images,” *Neuroimage*, vol. 14, no. 6, pp. 1454–1462, 2001.
- [60] S. M. Smith, M. Jenkinson, H. Johansen-Berg, D. Rueckert, T. E. Nichols, C. E. Mackay, K. E. Watkins, O. Ciccarelli, M. Z. Cader, P. M. Matthews, and T. E. J. Behrens, “Tract-based spatial statistics: Voxelwise analysis of multi-subject diffusion data,” *Neuroimage*, vol. 31, no. 4, pp. 1487–1505, 2006.
- [61] D. Wassermann, Y. Rathi, S. Bouix, M. Kubicki, R. Kikinis, M. Shenton, and C.-F. Westin, “White matter bundle registration and population analysis based on Gaussian processes,” *Information Processing in Medical Imaging*, vol. 22, pp. 320–332, 2011.
- [62] M. Walsh, C. A. Montojo, Y.-S. Sheu, S. A. Marchette, D. M. Harrison, S. D. Newsome, F. Zhou, A. L. Shelton, and S. M. Courtney, “Object working memory performance depends on microstructure of the frontal-occipital fasciculus,” *Brain Connect.*, vol. 1, no. 4, pp. 317–29, 2011.
- [63] J. D. Yeatman, R. F. Dougherty, N. J. Myall, B. A. Wandell, and H. M. Feldman, “Tract Profiles of White Matter Properties: Automating Fiber-Tract Quantification,” *PLoS One*, vol. 7, no. 11, 2012.
- [64] S. Mori, B. J. Crain, V. P. Chacko, and P. C. M. van Zijl, “Three-dimensional

- tracking of axonal projections in the brain by magnetic resonance imaging,” *Ann. Neurol.*, vol. 45, no. 2, pp. 265–269, 1999.
- [65] S. Wakana, A. Caprihan, M. M. Panzenboeck, J. H. Fallon, M. Perry, R. L. Gollub, K. Hua, J. Zhang, H. Jiang, P. Dubey, A. Blitz, P. van Zijl, and S. Mori, “Reproducibility of quantitative tractography methods applied to cerebral white matter,” *Neuroimage*, vol. 36, no. 3, pp. 630–644, 2007.
- [66] K. Hua, J. Zhang, S. Wakana, H. Jiang, X. Li, D. S. Reich, P. A. Calabresi, J. J. Pekar, P. C. M. van Zijl, and S. Mori, “Tract probability maps in stereotaxic spaces: Analyses of white matter anatomy and tract-specific quantification,” *Neuroimage*, vol. 39, no. 1, pp. 336–347, 2008.
- [67] B. A. Landman, J. A. D. Farrell, C. K. Jones, S. A. Smith, J. L. Prince, and S. Mori, “Effects of diffusion weighting schemes on the reproducibility of DTI-derived fractional anisotropy, mean diffusivity, and principal eigenvector measurements at 1.5T,” *Neuroimage*, vol. 36, no. 4, pp. 1123–1138, 2007.
- [68] H. Jiang, P. C. M. Van Zijl, J. Kim, G. D. Pearlson, and S. Mori, “DtiStudio: Resource program for diffusion tensor computation and fiber bundle tracking,” *Comput. Methods Programs Biomed.*, vol. 81, no. 2, pp. 106–116, 2006.

Chapter 2

Development, Implementation, and Validation of a Medial Axis Extraction Algorithm for Complex 3D Objects

Abstract

A medial axis (or skeletonization) is one of the most compact ways to present a digital image. However, although extracting the medial axis from a 2D image is relatively straight forward, the problem is substantially more complex for 3D objects (especially ones that are not smooth and/or uniform). In this paper, we present a novel methodology for computing the medial axis/skeleton of a discrete binary object using a ‘divide and conquer’ algorithm, in which any 3D object is first sliced into a series of 2D images in X, Y and Z directions. Then, a geometric (Voronoi) algorithm is applied to each 2D image to extract the respective medial axis. This information is then combined to reconstruct the medial axis of the original 3D object using an intersection technique. We then validated our approach using both standard benchmark 3D images, as well as more complex

medical images. The proposed algorithm consistently performed well, provided that the 3D input objects were smooth and continuous; however, for more complex 3D objects, the algorithm occasionally failed by leaving discontinuities (holes) in the extracted 3D skeleton. Therefore, to deal with such cases, we also implemented an optional 3D interpolation step that can be performed to achieve continuous connected skeletons. Briefly, this novel interpolation algorithm uses Delaunay triangles and a spherical search to establish the nearest neighboring points in 3D space for interpolation. Test results show that the proposed 3D Voronoi and optional interpolation algorithms can accurately and efficiently extract medial axes for complex 3D objects as well. In this paper, each of the aforementioned algorithms and the overall approach for 3D medial axis extraction are discussed in detail, the code (implemented in Matlab) is made freely available, and several examples are shown.

2.1 Introduction

The medial axis (or “topological skeleton”) of an object, first described by Blum [1], can be defined as the set of points within the object that are equidistant from two or more closest points along the object's boundary. An accurate skeleton is a highly efficient way to represent the topology of 2D or 3D objects in a compact way [2, 3] and has been widely used in various fields such as image processing and analysis, video graphics, character reconstruction, recognition and matching [4, 5].

Extraction of the medial axis or medial axis transform (MAT) for 2D/3D objects has typically been performed by one of the following three methods [6]: 1) boundary

removal, 2) distance map suppression or 3) geometric methods.

Boundary removal, also known as morphological thinning [7, 8, 9], is an iterative process of removing the border (outer edge) of an object, starting from the outside and moving toward the center, until the medial axis is extracted. Different thinning algorithms have been described [10], but most of these are an approximation of the grassfire process [11] that work like peeling an onion to reach its core. All pixels/voxels are removed except those whose removal affects the topology of an object [12, 13]. However, there are several drawbacks to this approach. The processing time increases with the size of the object because each pixel/voxel must be evaluated independently [14]; and both the accuracy of the estimated skeleton and the processing time depend critically on how many neighboring pixels (e.g., 4 vs. 8) or voxels (6 vs. 26) are considered during the thinning process [1, 15]. Generally speaking, accounting for more neighboring pixels/voxels, yields a more accurate representation of the medial axis, but including more neighbors means that processing time will also increase. Also, different thinning algorithms produce different skeletons when applied to the same image [10]. And finally, because it is an iterative process, an appropriate stopping criterion needs to be defined *a priori*, which may not be trivial.

On the other hand, distance transforms (DT) can be used to extract the medial axis by creating a distance map of an object [16, 17]. The distance map is created by assigning each pixel of an object value that is determined by its distance to the closest boundary [18], based on a predetermined distance calculation method (e.g., Euclidean [19], chessboard [20], city block [19], etc.). After creating the distance map, the medial axis is then extracted by suppressing pixels with a non-maximum distance [15], since (by

definition) pixels in the middle have the largest distance from the boundary. This process is also known as ridge detection [21] and is done using local/global adaptive thresholding approaches or gradient-based methods. This is a relatively fast and straightforward process compared to boundary removal. However, the main drawback is that the resulting medial axis may not be one-pixel thin, or that holes/discontinuities can sometimes appear in the resulting skeleton.

Finally, medial axes can be extracted using geometry-based algorithms such as Voronoi diagrams [22, 23, 24, 25], where the original object is first divided into polygons, and the centers of those polygons are subsequently determined using maximal disks. Skeletonization based on Voronoi diagrams is very robust, and often produces a skeleton that is one-pixel thin, continuous, and maintains the topology of the original object. The Voronoi method also has the advantage of being computationally efficient and is, therefore, faster than boundary removal or distance transform methods for large and/or complex objects [26]. The primary drawback of this approach is that the extracted skeleton may contain additional/redundant information due to the presence of noise; however, this can be removed using various pruning methods [27, 28, 29]. The main pipeline for all the three categories is shown in Figure 2-1.

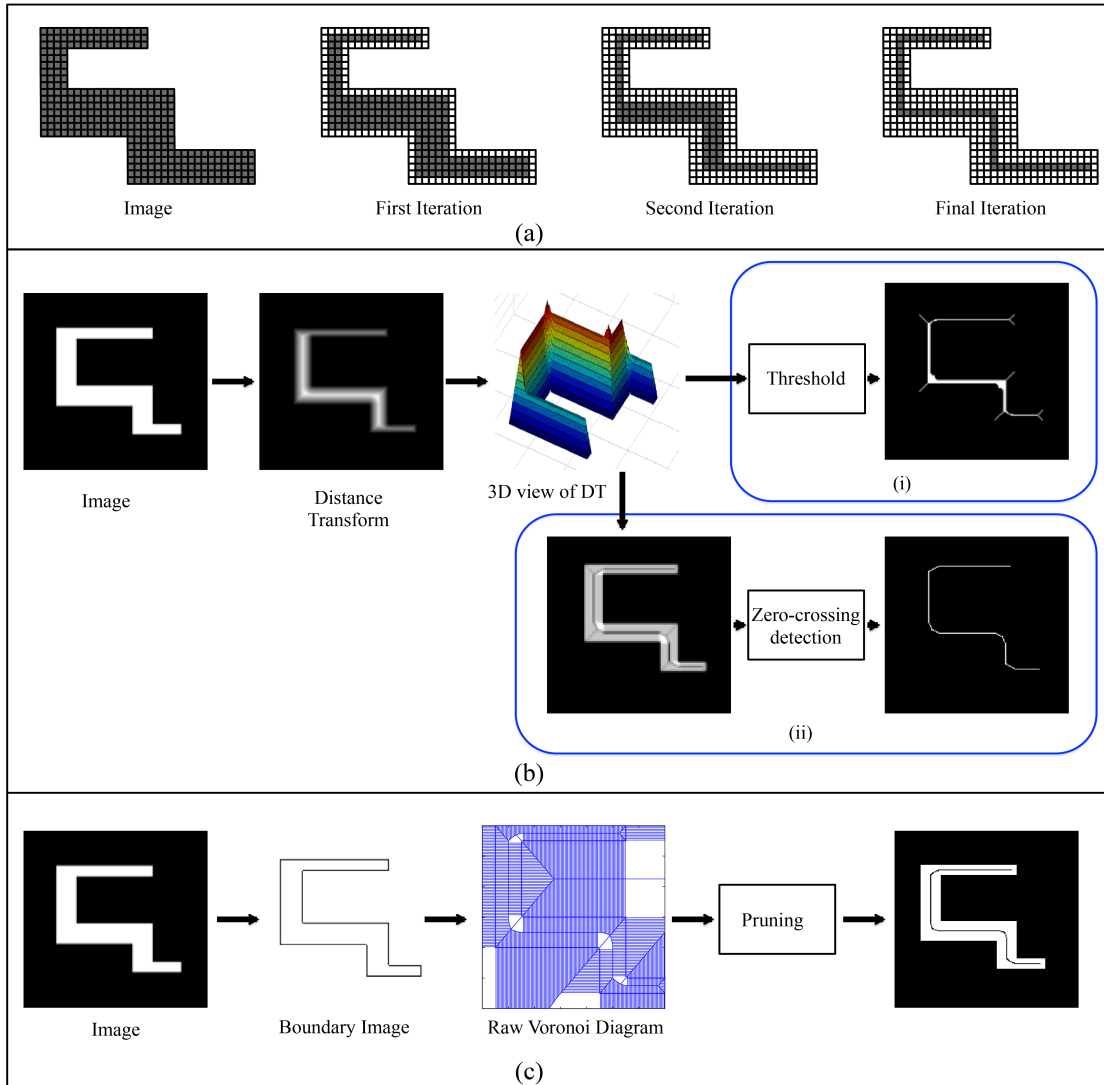


Figure 2-1: Main pipeline for different skeletonization algorithms (a) Boundary removal, in which the boundary is removed iteratively until the medial axis is extracted. (b) Distance Transform, in which each pixel is assigned a distance relative to its closest boundary, followed by thresholding to detect ridges (high-assigned distances) or trough (zero-crossing pixels). (c) Voronoi Diagram, in which the object is divided into polygons, and the medial axis is extracted using a pruning technique.

2.2 Preliminary Description of Voronoi Diagrams

According to the definition of a Voronoi diagram, the space S between two points

p_1 and p_2 is equally divided with the help of the bisector E , that passes perpendicularly at the center of the line segment joining points p_1 and p_2 [30, 31], as shown in Figure 2-2(a). Similarly, space S having many points P (also called sites) can be equally divided into Voronoi regions (also called Voronoi cells) among these points P . Each Voronoi cell, which is a convex polygon, will have only one site within it and any points on its boundaries, called Voronoi edges, are equidistant from exactly two sites. Intersection of three Voronoi edges will give rise to a Voronoi vertex, which is equidistant from exactly three sites. Thus, a Voronoi diagram is the final result of partitioning an object into Voronoi cells.

Different algorithm can be used to calculate the Voronoi diagram of n sites. These algorithms include a lower bound [32, 33], incremental construction [34] whose efficient implementation was done by Ohya [35] and Sugihara [36], divide & conquer [37] and a well-known sweep algorithm [38].

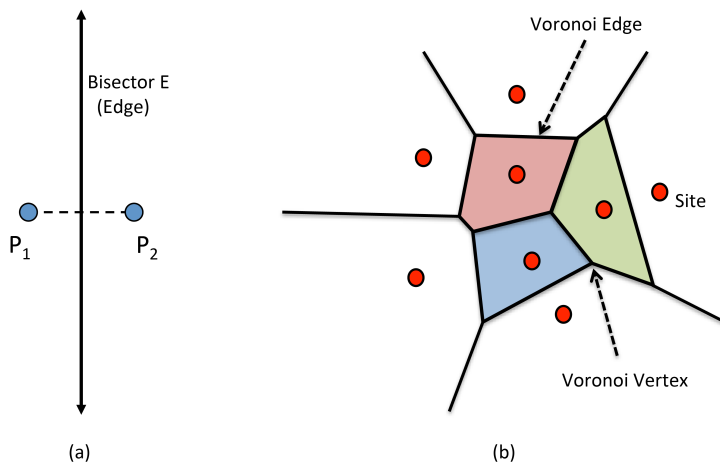


Figure 2-2: (a) Division of space between two points. (b) Voronoi diagram of n sites and its main components. Notice that the colored polygons (red, green and blue) are bounded cells, whereas others are unbounded cells.

2.3 2-D Methodology Description of Voronoi Diagrams

Our 3D medial axis extraction algorithm builds on previously described 2D approaches. Therefore, we will first explain the steps using 2D images, and then the concept will be further extended for 3D images in the next section.

2.3.1 Voronoi Diagram of a 2D Image

Assuming that there is only one object present in the image whose medial axis is being extracted, all points of the medial axis are centered with respect to the boundaries of that object. Therefore, before the Voronoi diagram can be generated, the object boundaries must be identified. Different edge detectors (e.g. Sobel or Canny or any other edge operator, details can be found in [39]) can be used to detect the boundary of an object within the image. Then, once the boundary of the object has been identified, space can be divided into Voronoi cells (as described above in Section 2.2).

2.3.2 Initial cleaning of the Raw Voronoi Skeleton

The raw Voronoi skeleton of an object contains branches that are clearly outside of the object's boundaries, but still within the image. These branches/segments do not have any significant value, as these are segments of unbounded polygons (as described previously in section 2.2). Therefore, initial cleaning has to be done to remove all of the segments that lie outside the object's boundaries.

2.3.3 Pruning the Raw Voronoi Skeleton

Due to the presence of noise in the boundary information, the resulting Voronoi

diagram of an object may not be considered a medial axis if it contains spurious branches. Therefore, pruning – i.e., the process of determining whether a particular branch of the skeleton is redundant or not, and if so, removing the redundant segment – may be necessary to eliminate these spurious branches and to extract the correct medial axis. The pruning process implemented in this paper compares the Euclidean distance between two sites with their contour distance along the boundary, as explained below [22].

Each Voronoi edge, a branch of the raw skeleton, is equidistant from exactly two sites (p_i & p_j) as mentioned earlier. These two sites can provide information about the Euclidean distance ($dist_E$) and contour distance ($dist_c$) between them. The Euclidean distance between two points (p_1 & p_2) having spatial coordinates (x_1, y_1) and (x_2, y_2) respectively, is calculated using the following equation.

$$dist_E = \sqrt{(x_1 - x_2)^2 + (y_1 - y_2)^2} \quad (2.1)$$

The Euclidean distance serves as the diameter of the maximal disk D_c , which can fit between those two sites (p_i & p_j) having these sites on its circumference. The area (D_A) and the circumference (D_C) of this maximal disk can be calculated using following equations:

$$D_A = T \cdot \left(\frac{dist_E}{2}\right)^2 \quad (2.2)$$

$$D_C = 2 T \cdot \left(\frac{dist_E}{2}\right) \quad (2.3)$$

where T is a control parameter with values less than, equal to, or greater than π (e.g., $\pi/3, \pi/2, 2\pi/3, \pi, 3\pi/2, 2\pi, 3\pi$, etc.). The effects of varying the magnitude of the

control parameter are demonstrated in the results section below.

The contour distance is the distance between two points while moving along the boundary of an object as shown in Figure 2-3. There are two pathways to calculate the contour distance between two points while running along the boundary. The minimum of the two contour distances is selected. Both the distances ($dist_E$ & $dist_c$) are shown in Figure 2-3.

$$dist_c = \min(dist_{c1}, dist_{c2}) \quad (2.4)$$

The Voronoi edge is considered to be spurious if the contour distance ($dist_c$) is less than the circumference D_C of the maximal disk with a diameter equal to the Euclidean distance, such that:

$$Voronoi\ edge = \begin{cases} spurious & dist_c < D_C \\ not\ spurious & otherwise \end{cases} \quad (2.5)$$

Figure 2-3 demonstrates how an edge is decided spurious or not. $Edge_x$, $edge_y$ and $edge_z$ are equidistant from sites (p_1 & p_2), (p_3 & p_4) and (p_5 & p_6), respectively. For $edge_x$ and $edge_y$, the minimum of their respective contour distance $dist_c$ is larger than the circumference of the circle having diameter equal to their respective sites' Euclidean distance. Therefore, these edges are not considered to be spurious and are not eliminated from the final accurate skeleton. However, the minimum contour distance for $edge_z$ is less than the circumference of the circle containing (p_5 & p_6), so this edge is considered spurious and is excluded from the final skeleton. After checking all the Voronoi edges, the refined skeleton is created as shown in Figure 2-4.

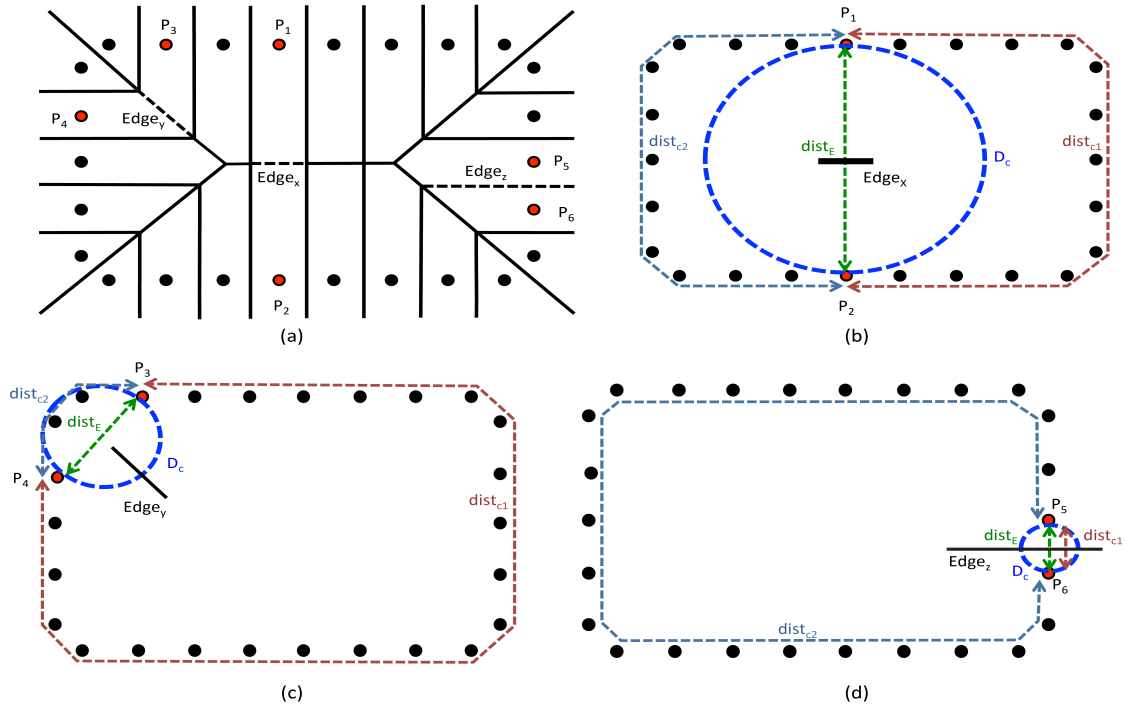


Figure 2-3: Demonstration of the Pruning Process. (a) Raw Voronoi Skeleton of boundary points (b) Pruning process for Edge X (c) Pruning process for edge Y (d) Pruning process for Edge Z. Light blue and light red lines show the contour distances, the green line shows the Euclidean distance, and the dark blue circle shows the circumference. If the circumference of the dark blue circle is greater than either the light blue or light red lines (i.e., the minimum of the two contour distances), the segment is considered to be spurious and will be removed from the final skeleton.

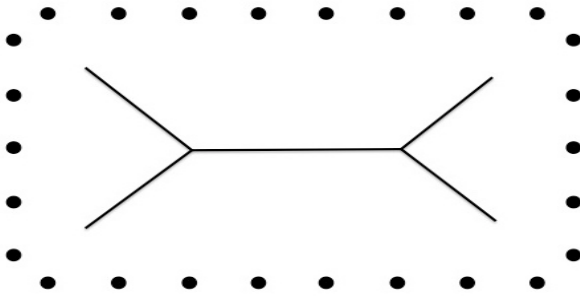


Figure 2-4: Refined skeleton after pruning process.

2.3.4 Summary

The procedure for medial axis extraction of a 2D image is given below, with the block diagram shown in Figure 2-5.

Step 1: Generate binary image.

Step 2: Boundary detection.

Step 3: Raw skeleton using Voronoi diagram algorithm.

Step 4: Initial cleaning process.

Step 5: Pruning of raw skeleton.

5.1: Pick Voronoi edge.

5.2: Find its corresponding sites.

5.3: Calculate the $dist_c$ and D_c .

5.4: Check for spurious edge using equation 5.

5.5: Refine the raw skeleton.

Step 6: Continue step 4 for all edges and generate medial axis.

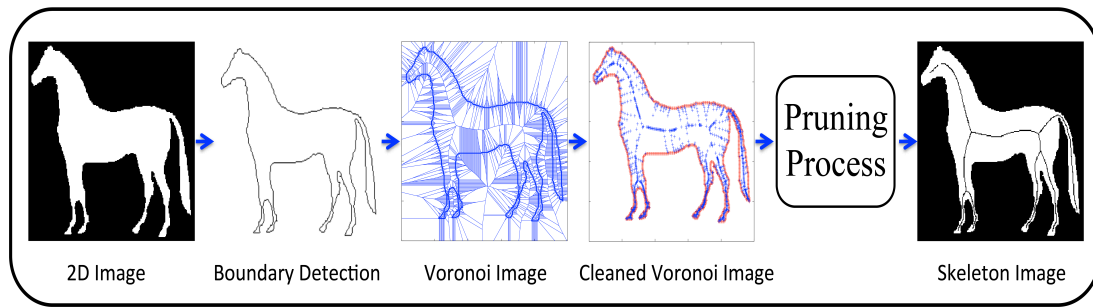


Figure 2-5: Block diagram of the 2D skeletonization procedure using a Voronoi diagram and pruning algorithm.

2.4 Interpolation

Given a set of distinct points $P = \{p_1, p_2, p_3 \dots p_n\}$ in any space, an ideal condition of interpolation would be to have these points P arranged in either ascending or descending order. Under such conditions, any spline method could then be used to interpolate between consecutive points. However, points along the medial axis are not inherently arranged in order, so this must be done before interpolation can be performed. One common method of finding nearest neighbors is based on Euclidean distance; since smaller Euclidean distances between points generally means that those points have a higher likelihood of being neighbors. However, Euclidean distance is not the only factor when tracing a path, and other than the end points, all other points in the path will have two nearest neighbors, so a more sophisticated approach is needed.

2.4.1 Nearest Neighbors Search Algorithm

Here we are proposing a novel technique for finding neighboring points if the given set of points P are not in order. Since Maus & Drange [40] proved that all closest neighbors are proper edges of their respective Delaunay triangles, we propose to identify

the edges of Delaunay triangles related to each point and to then apply a circular algorithm to identify the nearest neighbor, as follows.

The triangle formed by any three points (p_i, p_j, p_k) from the given points in P are considered to be a Delaunay triangle if the circumscribed circle of this triangle does not contain any other points from P and these points p_i, p_j and p_k are on its circumference [40, 41, 42]. Figure 2-6(a) shows the Delaunay triangulation D of the points P having $(p_1, p_2, p_3, p_4, p_5, p_6, p_7)$. The points P are not in sequence; so direct interpolation would yield incorrect results. Therefore, these points are first arranged according to their closest neighbors. Figure 2-6(b) and 2-6(c) show the Delaunay edges with respect to point p_1 and p_2 , and all of the Delaunay edges with respect to every other point can be obtained in the same way.

Nearest neighbors can be found by checking each Delaunay edge using a circular algorithm [43]. According to this algorithm, points p_i and p_j are nearest neighbors if (and only if) no other points in P fall inside the circle bisected by the Delaunay edge between those points (p_i & p_j). Otherwise, if any other points fall within the circle, they are not considered to be nearest neighbors.

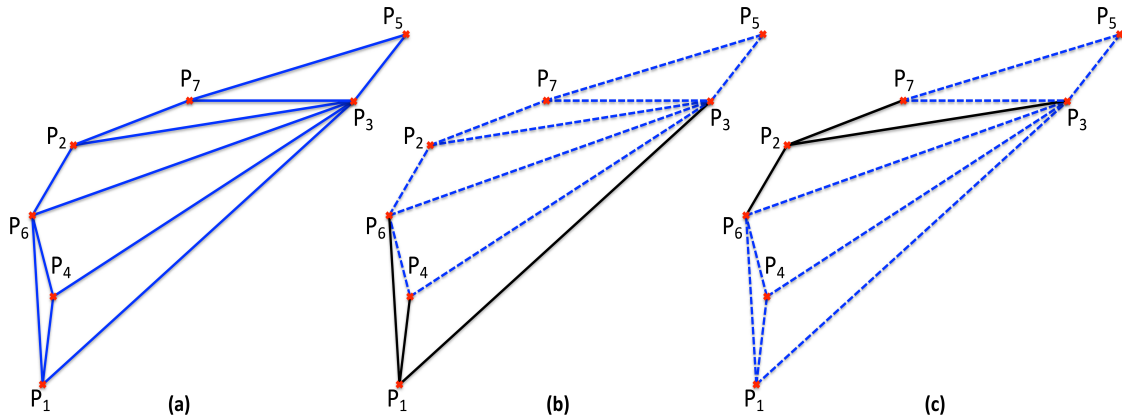


Figure 2-6: Delaunay triangles for n points. (b) Triangle edges with respect to point p_1 . (c) Triangle edges with respect to point p_2 .

Figure 2-7 demonstrates how the algorithm works for point p_1 . Delaunay triangles indicate that p_1 makes triangle edges with points p_3, p_4 and p_6 . It can be seen that points p_1 & p_3 are not nearest neighbors because several other points (p_2, p_4, p_6, p_7) from P fall inside the circle having diameter \mathbf{d} (defined by the edge connecting p_1 & p_3). Similarly, the condition fails for points p_1 & p_6 because another point (p_4) from P lies inside the circle having diameter \mathbf{d} (defined by the edge between p_1 & p_6). This proves that p_1 is not a nearest neighbor of p_3 or p_6 . However, points p_1 and p_4 are nearest neighbors because no other points from P fall inside the circle formed by p_1 and p_4 (as shown in Figure 2-7).

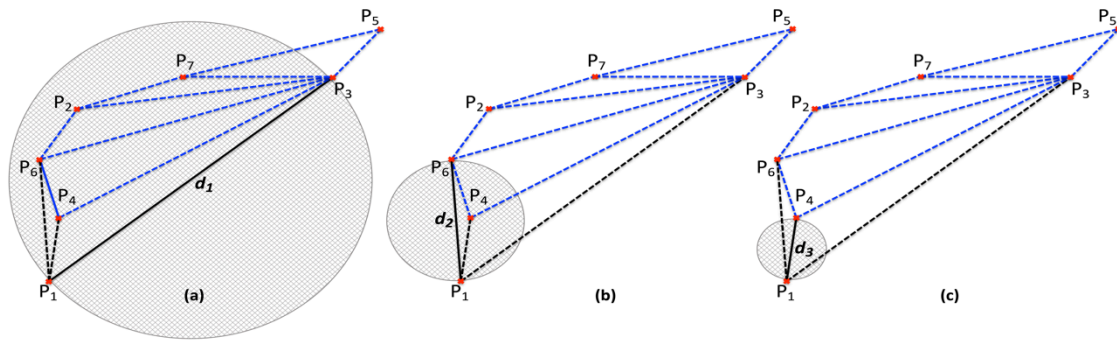


Figure 2-7: Demonstration of the nearest neighbor search algorithm with respect to point P_1 .

Likewise, out of the three Delaunay edges for point p_2 (i.e., connecting to points p_3, p_6 and p_7), points p_6 and p_7 are nearest neighbors on either side because no other points from P fall inside the circles bisected by either edge (Figure 2-8b,c). However, p_3 is not considered to be a nearest neighbor of p_2 , because another point (p_7) lies inside the circle bisected by the edge connecting p_2 and p_3 (as shown in Figure 2-8a).

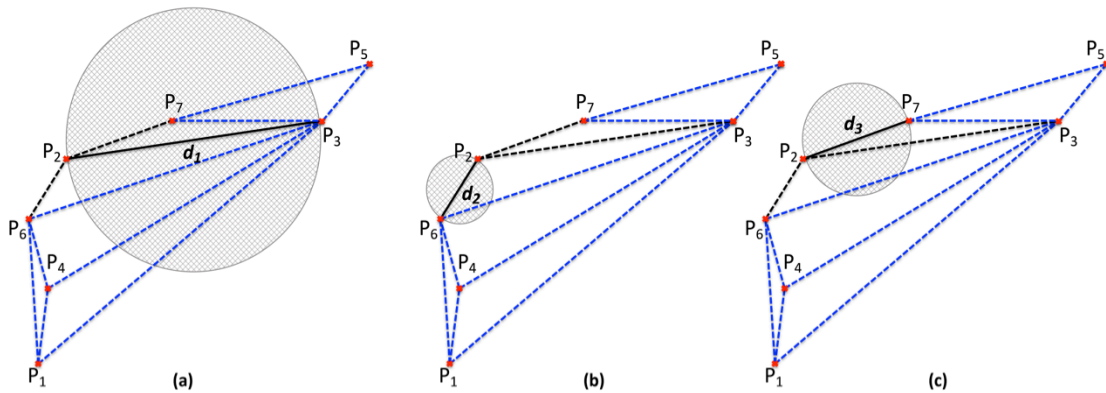


Figure 2-8: Demonstration of the nearest neighbor search algorithm with respect to point P_2 .

After checking each Delaunay triangle edge with respect to every starting point, only those edges are kept which satisfy the aforementioned nearest neighbor condition. Figure 2-9 shows that $P(p_1, p_2, p_3, p_4, p_5, p_6, p_7)$ can be easily arranged according to their nearest neighbors, where the arranged points are $(p_1, p_4, p_6, p_2, p_7, p_3, p_5)$. Once the points are arranged, then interpolation can be done between each nearest neighbor pair by

using any desired interpolation technique. In 3D space, spherical checks are performed instead on circular checks.

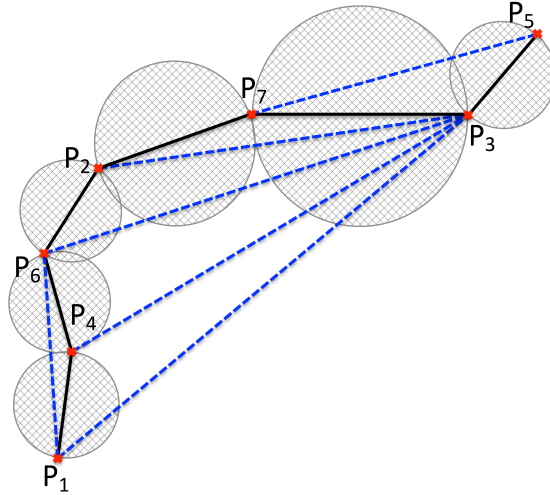


Figure 2-9: Final result of the nearest neighbor algorithm.

2.5 3-D Methodology

The concepts applied for 2D medial axis extraction (discussed above in section 2.3), can also be expanded to extract the medial axis of any continuous 3D image. As previously discussed, 3D images can be divided into multiple 2D images – which allows the 2D algorithms to be applied (separately) on each 2D image – before finding the common intersection points of the 2D images, which represent the medial axis of the original 3D image [44].

In our implementation, we used a similar ‘divide and conquer’ approach for 3D medial axis extraction, but with a few modifications. First, the 3D image is sliced into multiple 2D images in the X, Y and Z directions (Figure 2.10). Then the Voronoi algorithm, discussed above, is used to extract the medial axis for each of the resulting 2D

images. After doing this, the extracted 2D medial axes are again stacked with their corresponding slicing direction to create their respective 3D medial axes (called the X-, Y- and Z-direction medial axes). The common skeleton between these three (X-, Y- and Z-direction) intermediate medial axis images is then determined from the intersections between any two directions (XY-, YZ-, ZX-common), as well as the intersections between all three directions (XYZ-common). Finally, each of the four resulting 3D medial axes are visually overlaid on the original 3D object and are assessed by the user (via visual examination) to select the best one – i.e., the one that most accurately represents the skeleton of the original object, is only one-pixel thick, and has the lowest amount of redundant information.

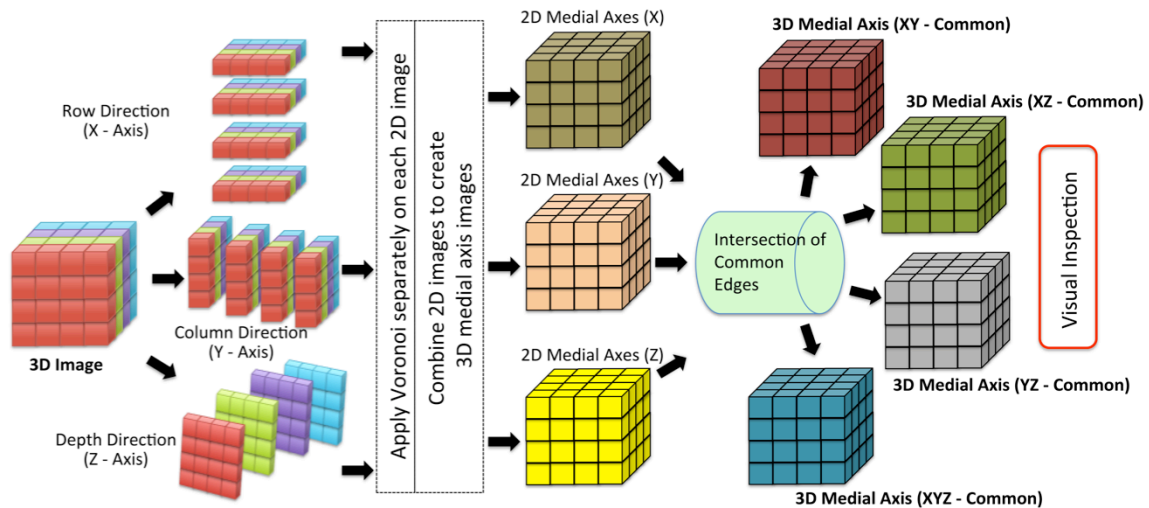


Figure 2-10: 3D medial axis extraction flow chart.

2.6 Result

Three experiments are designed to test the performance of the algorithm discussed above. The first experiment evaluated the pruning process and the effects of control

parameter T for removing excess medial axis branches, and also confirmed the stability of the Voronoi algorithm on standard 2D images. The second and third experiments then evaluated the overall performance of the 3D medial axis extraction algorithm on regular (i.e., smooth and continuous) 3D objects and highly complex 3D diffusion tensor magnetic resonance images (i.e., to illustrate potential applications to other 3D medical images), respectively. Each of these is discussed in detail below.

2.6.1 Experiment 1

The control parameter T used in (3) controls the strictness of the pruning process by determining the number of branches that are retained in the final extracted skeleton. In this case, lower values of π (e.g., $\pi/3$, $\pi/2$, $2\pi/3$) will retain more branches in the skeleton, while using higher values of π (such as 2π) will remove more branches from the skeleton. Figure 2-11 shows the effect of different values of π on the skeleton.

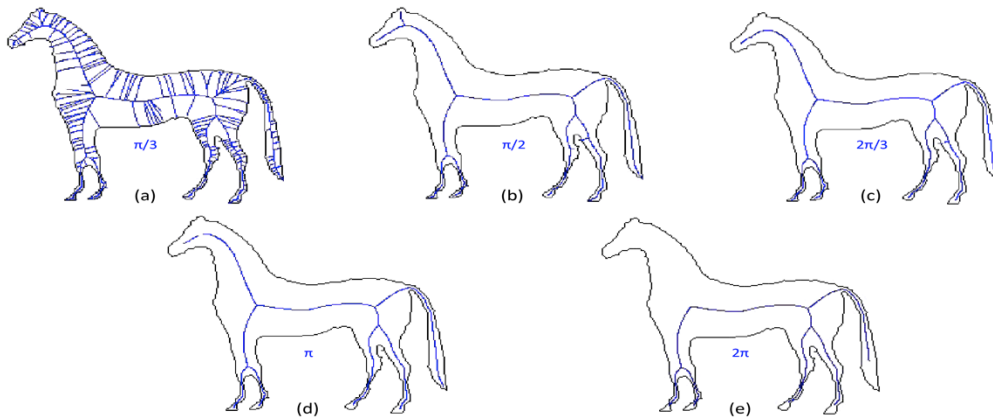


Figure 2-11: Effect of T on the medial axis pruning (a) at $\pi/3$ (b) at $\pi/2$ (c) at $2\pi/3$ (d) at π (e) at 2π .

The stability of the Voronoi algorithm was then tested on a random assortment of 2D binary images taken from the benchmark MPEG-7 database [45]. For this experiment,

we used different variations of the control parameter to extract the skeleton of the respective image. Figure 2-12 shows the results, which prove that the implemented 2D Voronoi algorithm accurately extracted the 2D skeletons for each image.

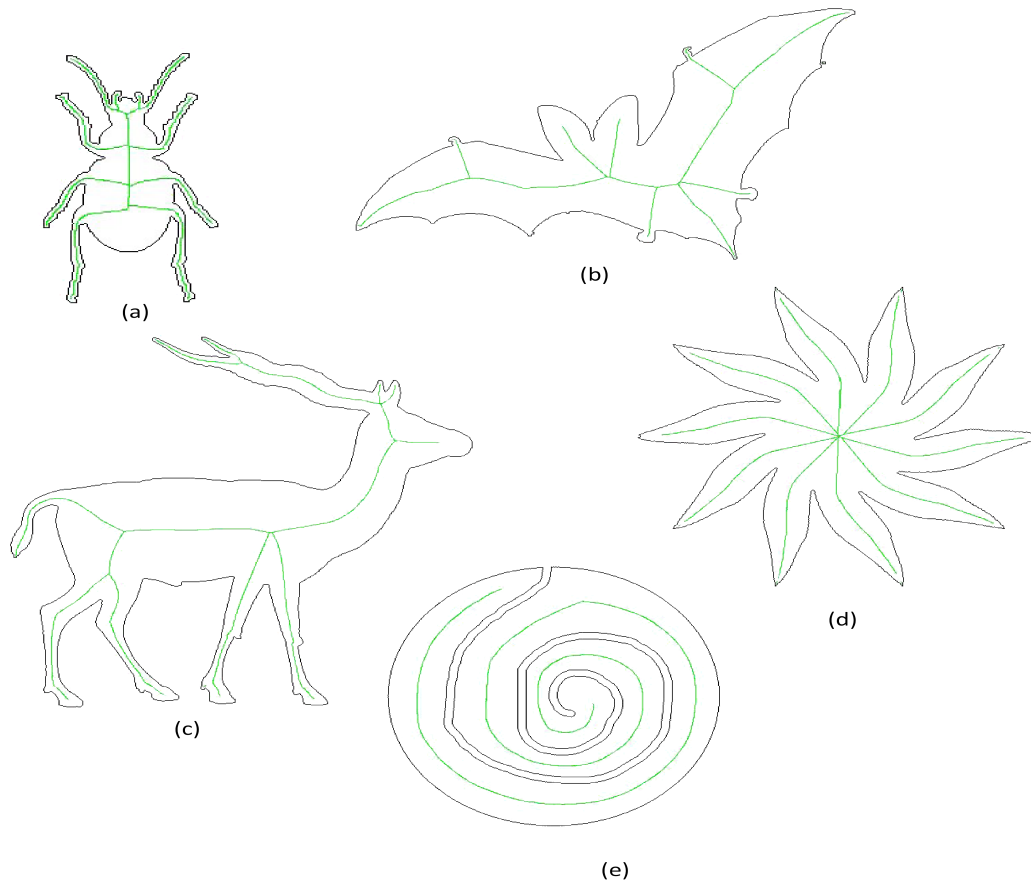


Figure 2-12: Results of 2D Voronoi Algorithms tested on five randomly selected images from the MPEG-7 database. (a) Beetle-11 at $2\pi/3$ (b) Bat-4 at $2\pi/3$ (c) Deer-6 at $2\pi/3$ (d) Device 7-3 at π (e) Device 9-6 at π . The green line shows the extracted medial axis for the respective images.

2.6.2 Experiment 2

In this experiment, we tested the complete Voronoi algorithm for 3D medial axis extraction on a random assortment of smooth and continuous 3D binary images from the McGill

3D Shape Benchmark database [46]. For each 3D image, the algorithm produced four possible medial axes (Figure 2-13), as discussed above in the methodology section. However, the most accurate among these (selected by visual examination) consistently demonstrated that our algorithm accurately extracted the connected medial axis and maintained the 3D topology of the original smoothed and continuous image (Figure 2-14).

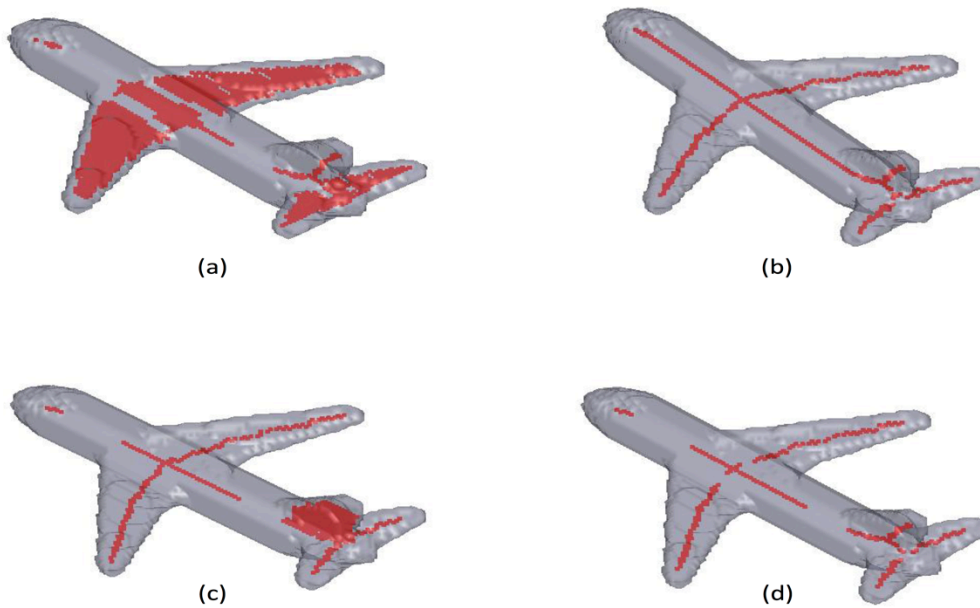


Figure 2-13: All four outputs from our 3D Medial Axis Algorithm (a) XY-common intersection (b) YZ-common intersection (c) ZX-common intersection (d) XYZ-common intersection. The medial axis formed by the YZ-common intersection (b) is the only skeleton that is continuous, one pixel thin, and preserves the topology of the input image. Therefore, the continuous and one-pixel thinned result can be easily (visually) identified by the user and saved as the correct medial axis.

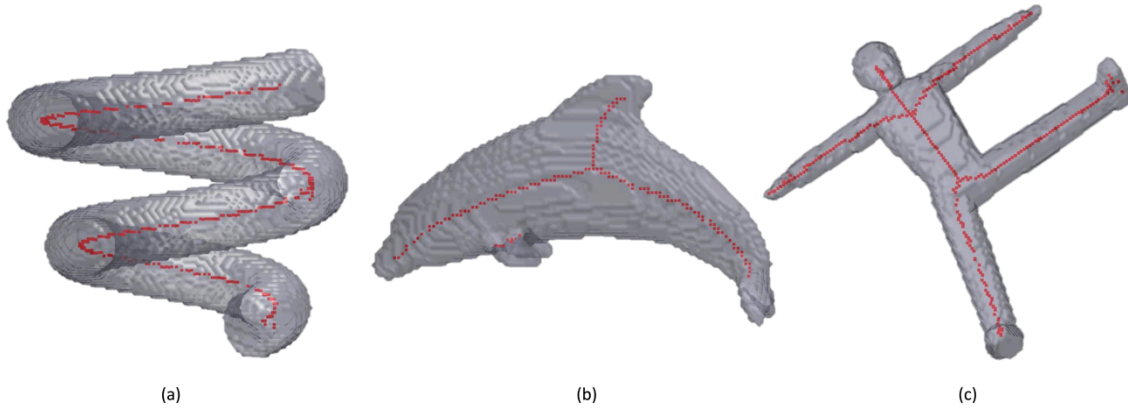


Figure 2-14: Typical results of our 3D Medial Axis Algorithm on other smooth, continuous 3D images. (a) Snake (b) Dolphin (c) Human. These were all extracted at $\pi/2$, and visual selection was performed to identify the correct output.

2.6.3 Experiment 3

After confirming that our 3D medial axis extraction algorithm consistently performed well on smooth and continuous 3D images, we wanted to identify whether it was robust enough for potential 3D medical imaging applications. Binary masks from medical images are more complicated than the previous benchmarking images due to lower resolution and less smooth, more irregular shapes. As a result, extracting medial axes for these kinds of images is a more complicated task.

In this experiment, we subjected our 3D medial axis extraction algorithm to a ‘stress test’ by evaluating its performance on human brain white matter atlases that were derived from diffusion tensor imaging data. Specifically, we chose a random assortment of fiber tracts from the UManitoba-JHU Functionally-Defined White Matter Atlas [47] to test the algorithm. As shown in Figure 2-15, the algorithm worked surprisingly well for most of the fiber tracts.

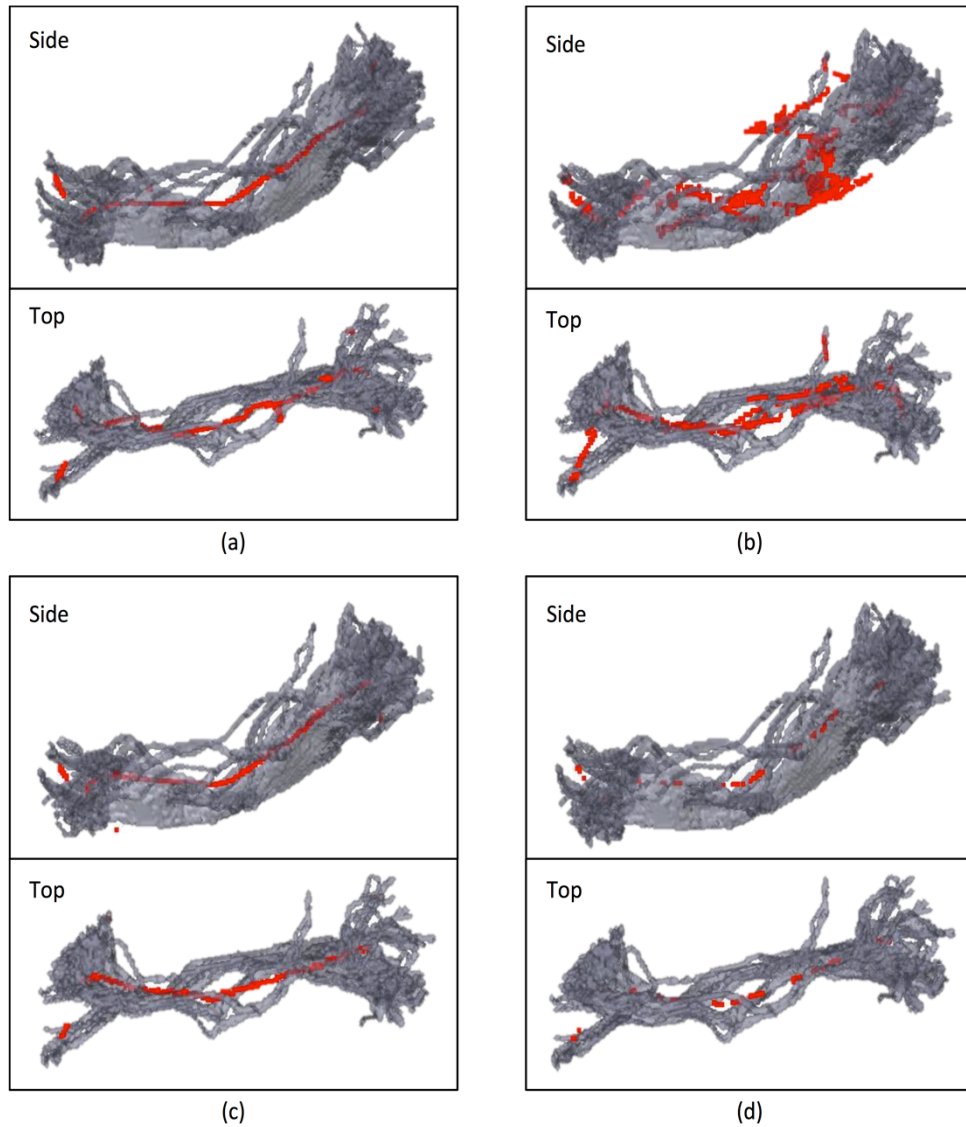


Figure 2-15: All four outputs from the 3D medial axis extraction algorithm. (a) XY-common intersection (b) YZ-common intersection (c) ZX-common intersection (d) XYZ-common intersection. Among these, only the ZX-common intersection (c) has a clean, continuous medial axis.

However, in some cases, the 3D Voronoi algorithm did not perform quite as well. It is evident in Figure 2-16 that none of the four outputs represent an accurate medial axis (since each one contains erroneous points and/or holes in the extracted skeleton).

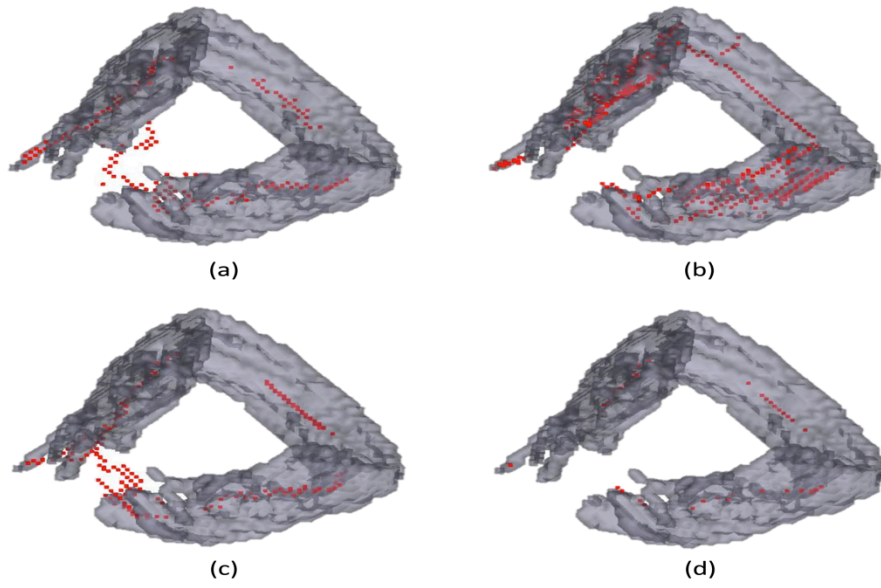


Figure 2-16: An example in which the 3D Voronoi algorithm failed to produce an accurate medial axis (since all four of the outputs contain either erroneous points or holes).

Therefore, this represents a situation in which the interpolation algorithm must be used. Although it is an approximation of the medial axis in the regions with missing data, interpolating to fill the holes in the XYZ-common medial axis effectively (Figure 2-16d) produces a continuous medial axis (Figure 2-17). Finally, other examples of white matter fibers requiring interpolation are shown in Figure 2-18.

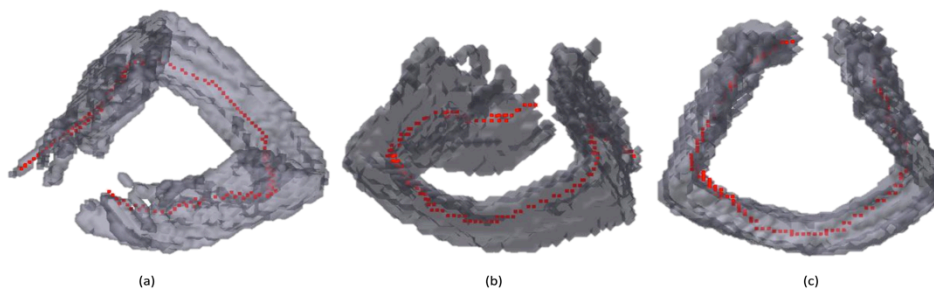


Figure 2-17: The resulting 3D skeleton after the interpolation algorithm was applied to the XYZ-common intersection. (a) Front view (b) Back view (c) Top view. Notice that the interpolation algorithm produced a continuous medial axis that mostly preserved the topology of the original image.

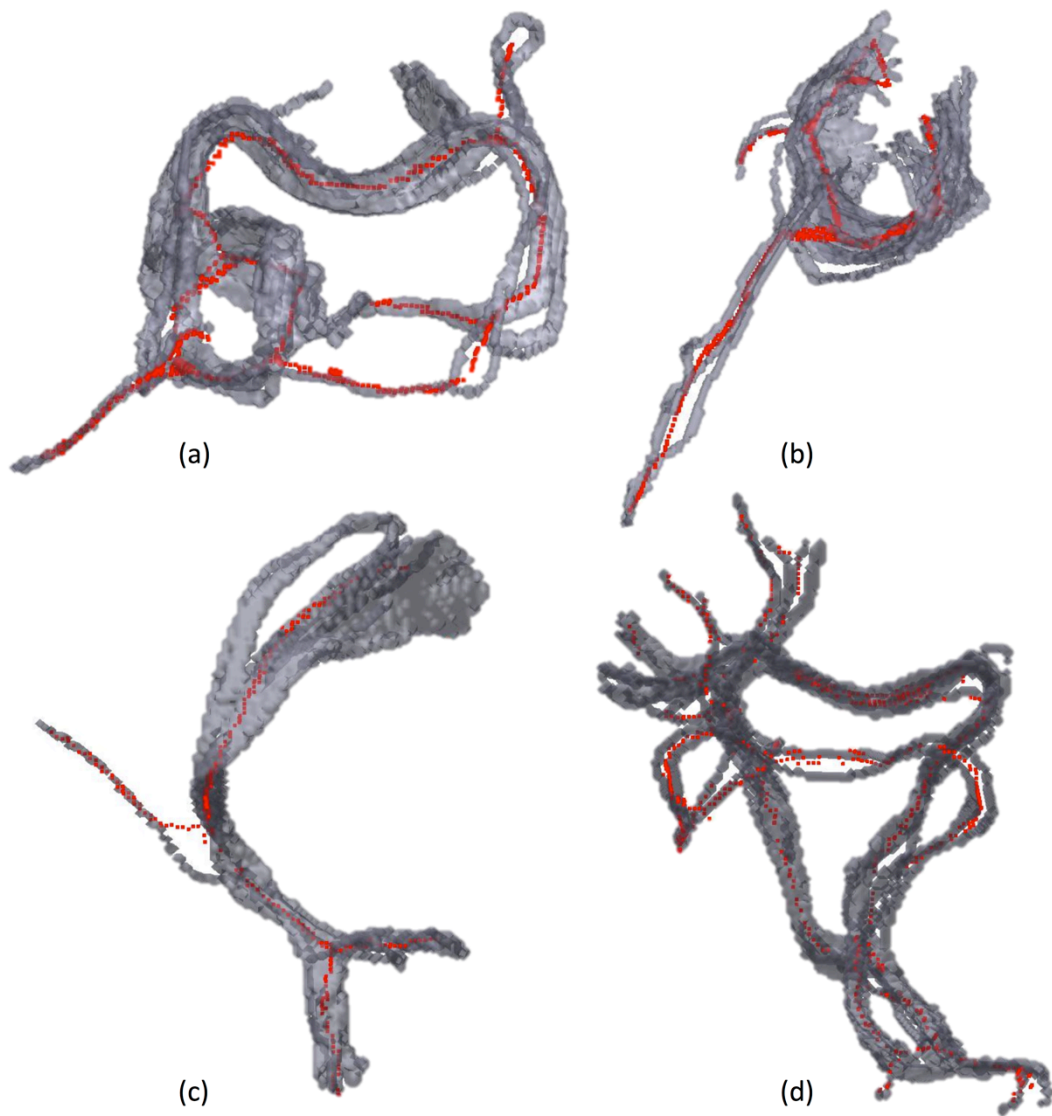


Figure 2-18: Testing results from other white matter atlases. (a) & (b) Results of 3D Voronoi Algorithm along with the interpolation algorithm. (c) Result took from ZX-common intersection. (d) Result from XYZ-common intersection.

2.7 Discussion

Overall, our results indicate that the proposed algorithm consistently extracts accurate medial axes from both 2D and 3D images and that the algorithm is even robust enough to remove 3D skeletons from sophisticated medical imaging data (especially when combined with the interpolation algorithm if necessary).

Although the interpolation algorithm has a relatively high computational cost compared to the initial 3D medial axis extraction algorithm, the overall processing times for both the benchmark (Table 2-1) and complex medical images (Table 2-2) are still reasonably fast with modern computers – especially given that most medical images are analyzed off-line. For example, the processing times in Tables 2-1 and 2-2 were benchmarked on a fairly ‘standard’ laptop with a 2.2 GHz Intel i7 Quad-Core processor.

Table 2-1: Processing times for smooth and continuous database objects.

Figure	Processing Time
	<i>Skeleton Extraction (seconds)</i>
2.13	8.11
2.14 (a)	32.62
2.14 (b)	10.02
2.14 (c)	9.31

Table 2-2: Processing times for white matter ROIs.

Figure	Processing Time	
	<i>Skeleton Extraction (seconds)</i>	<i>Interpolation (seconds)</i>
2.15	71.29	Not Required
2.16 & 2.17	15.17	94.72
2.18 (a)	43.64	1038.68
2.18 (b)	31.46	702.96
2.18 (c)	24.18	Not Required
2.18 (d)	44.53	Not Required

2.8 Conclusion

In this paper, we have developed and validated an algorithm for extracting medial axes from 3D images. The algorithm is based on a ‘divide and conquer’ approach, in which 3D images are first sliced along three different axes (height, width, and depth) to create a series of 2D images in each plane. A Voronoi algorithm is then applied to determine the medial axis of each 2D slice before the sliced images are recombined using an intersection technique to produce 3D medial axes images. An optional 3D interpolation algorithm has also been implemented to ensure that a continuous 3D medial axis can be extracted, even from complex 3D images (e.g., medical images). Finally, this algorithm has been implemented in Matlab and is freely available through Matlab Central.

2.9 References

- [1] H. Blum and R. N. Nagel, "SYMMETRIC AXIS FEATURES," *Pattern Recognit.*, vol. 10, pp. 167–180, 1978.
- [2] A. Sudhalkar, L. Gursijzt, and F. Prinzt, "Box-skeletons of discrete solids," *Comput. Des.*, vol. 26, pp. 507–517, 1966.
- [3] D. J. Sheehy, C. G. Armstrong, and D. J. Robinson, "Shape description by medial surface construction," *IEEE Trans. Vis. Comput. Graph.*, vol. 2, no. 1, pp. 62–72, 1996.
- [4] S. Tian, P. Shivakumara, T. Q. Phan, and C. L. Tan, "Scene character reconstruction through medial axis," in *Proceedings of the International Conference on Document Analysis and Recognition, ICDAR*, 2013, pp. 1360–1364.
- [5] S. Tian, P. Shivakumara, T. Q. Phan, T. Lu, and C. L. Tan, "Character shape restoration system through medial axis points in video," *Neurocomputing*, vol. 161, pp. 183–198, 2015.
- [6] S. Pizer, K. Siddiqi, and P. Yushkevich, *Medial Representations*, vol. 37. 2008.
- [7] P. A. Maragos and R. W. Schafer, "Morphological Skeleton Representation and Coding of Binary Images," *IEEE Trans. Acoust.*, vol. 34, no. 5, pp. 1228–1244, 1986.
- [8] B. K. Jang and R. T. Chin., "One-pass parallel thinning analysis, properties, and quantitative evaluation," *EEE Trans. Pattern Anal. Mach. Intell.*, vol. 11, pp. 1129–1140, 1992.
- [9] L. Lam and C. Y. Suen, "Evaluation of parallel thinning algorithms for character

- recognition,” *IEEE Trans. Pattern Anal. Mach. Intell.*, vol. 17, no. 9, pp. 914–919, 1995.
- [10] L. Lam and S. W. Lee, “Thinning methodologies—a comprehensive survey,” *IEEE Transactions on Pattern Analysis and Machine Intelligence*, vol. 14, no. 9, pp. 869–885, 1992.
- [11] C. J. Hilitch, “Linear Skeletons From Square Cupboards,” *Mach. Intell.* 4, pp. 403–420, 1969.
- [12] W. Xie, R. P. Thompson, and R. Perucchio, “A topology-preserving parallel 3D thinning algorithm for extracting the curve skeleton,” *Pattern Recognit.*, vol. 36, no. 7, pp. 1529–1544, 2003.
- [13] Y. Zhou and A. W. Toga, “Efficient skeletonization of volumetric objects,” *IEEE Trans. Vis. Comput. Graph.*, vol. 5, no. 3, pp. 196–209, 1999.
- [14] W. P. Choi, K. M. Lam, and W. C. Siu, “Extraction of the Euclidean skeleton based on a connectivity criterion,” *Pattern Recognit.*, vol. 36, no. 3, pp. 721–729, 2003.
- [15] F. Leymarie and M. D. Levine, “Simulating the Grassfire Transform Using an Active Contour Model,” *IEEE Trans. Pattern Anal. Mach. Intell.*, vol. 14, no. 1, pp. 56–75, 1992.
- [16] N. Ahuja and J. H. Chuang, “Shape representation using a generalized potential field model,” *IEEE Trans. Pattern Anal. Mach. Intell.*, vol. 19, no. 2, pp. 169–176, 1997.
- [17] H. Xia and P. G. Tucker, “Fast equal and biased distance fields for medial axis transform with meshing in mind,” *Appl. Math. Model.*, vol. 35, no. 12, pp. 5804–

5819, 2011.

- [18] R. Kimmel and R. . Maurer, “Method of computing sub-pixel euclidean distance maps,” 2003.
- [19] P. E. Danielsson, “Euclidean distance mapping,” *Comput. Graph. Image Process.*, vol. 14, no. 3, pp. 227–248, 1980.
- [20] C. Arcelli and G. S. Di Baja, “A width-independent fast thinning algorithm.,” *IEEE Trans. Pattern Anal. Mach. Intell.*, vol. 7, no. 4, pp. 463–474, 1985.
- [21] J. M. Gauch and S. M. Pizer, “Multiresolution Analysis of Ridges and Valleys in Grey-Scale Images,” *IEEE Trans. Pattern Anal. Mach. Intell.*, vol. 15, no. 6, pp. 635–646, 1993.
- [22] R. L. Ogniewicz and O. Kubler, “Hierarchic Voronoi skeletons,” *Pattern Recognit.*, vol. 28, no. 3, pp. 343–359, 1995.
- [23] N. Mayya and V. T. Rajan, “Voronoi diagrams of polygons: A framework for shape representation,” *Comput. Vis. Pattern Recognition, 1994. Proc. CVPR '94., 1994 IEEE Comput. Soc. Conf.*, vol. 378, pp. 1–32, 1994.
- [24] N. Mayya and V. T. Rajan, “An efficient shape representation scheme using Voronoi skeletons,” *Pattern Recognit. Lett.*, vol. 16, no. 2, pp. 147–160, 1995.
- [25] J. W. Brandt and V. R. Algazi, “Continuous skeleton computation by Voronoi diagram,” *CVGIP Image Underst.*, vol. 55, no. 3, pp. 329–338, 1992.
- [26] P. K. Saha, G. Borgefors, and G. Sanniti di Baja, “A survey on skeletonization algorithms and their applications,” *Pattern Recognit. Lett.*, vol. 76, pp. 3–12, 2016.
- [27] H. Liu, Z.-H. Wu, X. Zhang, and D. F. Hsu, “A skeleton pruning algorithm based on information fusion,” *Pattern Recognit. Lett.*, vol. 34, no. 10, pp. 1138–1145,

2013.

- [28] N. Amenta and R. K. Kolluri, “The medial axis of a union of balls,” *Comput. Geom. Theory Appl.*, vol. 20, no. 1–2, pp. 25–37, 2001.
- [29] F. Mokhtarian and A. K. Mackworth, “A theory of multiscale, curvature-based shape representation for planar curves.pdf,” *IEEE Transactions on Pattern Analysis and Machine Intelligence*, vol. 14, no. 8. p. 789, 1992.
- [30] F. Aurenhammer, “Voronoi diagrams,” *ACM Comput. Surv.*, vol. 23, no. 3, p. 94, 1991.
- [31] F. Aurenhammer, “Voronoi Diagrams — A Survey of a Fundamental Data Structure,” *ACM Comput. Surv.*, vol. 23, no. 3, pp. 345–405, 1991.
- [32] L. Guibas and J. Stolfi, “Primitives for the manipulation of general subdivisions and the computations of Voronoi diagrams,” *ACM Tmns. Graph*, vol. 4, no. April, pp. 74–123, 1985.
- [33] D. E. Muller and F. P. Preparata, “Finding the intersection of two convex polyhedra,” *Theor. Comput. Sci.*, vol. 7, no. 2, pp. 217–236, 1978.
- [34] P. J. Green and R. Sibson, “Computing dirichlet tessellations in the plane,” *Comput. J.*, vol. 21, no. 2, pp. 168–173, 1978.
- [35] T. Ohya, M. Iri, and K. Murota, “Improvements of the incremental method for the Voronoi diagram with computational comparison of various algorithms,” *J. Oper. Res. Soc. Japan.*, vol. 27, no. 4, pp. 306–336, 1984.
- [36] K. Sugihara and M. Iri, “Construction of the Voronoi Diagram for ‘One Million’ Generators in Single-Precision Arithmetic,” *Proc. IEEE*, vol. 80, no. 9, pp. 1471–1484, 1992.

- [37] M. I. Shamos and D. Hoey, "Closest-point problems," *Found. Comput. Sci. 1975., 16th Annu. Symp.*, pp. 151–162, 1975.
- [38] K. Q. Brown, "Algorithms for Reporting and Counting Geometric Intersections," *IEEE Trans. Comput.*, vol. C–30, no. 2, pp. 147–148, 1981.
- [39] H. Spontón and J. Cardelino, "A Review of Classic Edge Detectors," *Image Process. Line*, vol. 5, pp. 90–123, 2015.
- [40] A. Maus and J. Drange, "All closest neighbors are proper Delaunay edges generalized, and its application to parallel algorit," *Nor. Inform.*, pp. 1–12, 2010.
- [41] M. De Berg, O. Cheong, M. Van Kreveld, and M. Overmars, *Computational Geometry: Algorithms and Applications*, vol. 17. 2008.
- [42] G. Farin, D. Hoffman, and C. R. Johnson, "Triangulations and Applications," *New York*, 2006.
- [43] D. T. Lee and B. J. Schachter, "Two algorithms for constructing a Delaunay triangulation," *Int. J. Comput. Inf. Sci.*, vol. 9, no. 3, pp. 219–242, 1980.
- [44] A. Telea and J. J. van Wijk, "An augmented Fast Marching Method for computing skeletons and centerlines," *Jt. EUROGRAPHICS - IEEE TCVG Symp. Vis.*, pp. 251–260, 2002.
- [45] X. Bai, X. Yang, L. J. Latecki, W. Liu, and Z. Tu, "Learning context-sensitive shape similarity by graph transduction," *IEEE Trans. Pattern Anal. Mach. Intell.*, vol. 32, no. 5, pp. 861–874, 2010.
- [46] K. Siddiqi, J. Zhang, D. MacRini, A. Shokoufandeh, S. Bouix, and S. Dickinson, "Retrieving articulated 3-D models using medial surfaces," *Mach. Vis. Appl.*, vol. 19, no. 4, pp. 261–275, 2008.

- [47] T. D. Figley, N. Bhullar, S. M. Courtney, and C. R. Figley, “Probabilistic atlases of default mode, executive control, and salience network white matter tracts: an fMRI-guided diffusion tensor imaging and tractography study,” *Front. Hum. Neurosci.*, vol. 9, no. November, p. Article 585, 2015.

Chapter 3

Quantitative Tract Integrity Profiles (Q-TIPs)

A Novel Matlab Toolbox for Assessing White Matter Integrity

Abstract

In this paper, we present a novel toolbox called “Quantitative Tract Integrity Profiles (Q-TIPs)” for performing tract-based analyses to quantify the integrity of white matter along tracts. Q-TIPs extracts the orientation of any ROI mask or atlas, that has already been created, using a novel medial axis extraction technique to identify the principal orientation along the ROI automatically. After extracting the medial axis, the cross-sectional planes are made to obtain any quantitative white matter imaging values (e.g. fractional anisotropy, mean diffusivity, T1w/T2w ratio, magnetization transfer ratio, etc.) along the fiber tract. Test results show that Q-TIPs efficiently extracts the medial

axis and performs cross-sectional slices of any provided ROI. In this paper, each of the previous mentioned quantitative techniques and all image processing steps involved in Q-TIPs are discussed in detail with several examples shown.

3.1 Introduction

Quantification of white matter tracts has long been studied under either region-of-interest (ROI) analysis or voxel-wise analysis. ROI analyses [1, 2, 3, 4] is hypothesis-driven studies, where a pre-defined region of interest is selected for a particular study. These are useful for studying global changes in cross-subject analyses, but sensitivity is reduced for small localized regions. On the other hand, voxel-wise analyses [5, 6] perform point-by-point statistical analyses, facilitating high spatial resolution. However, voxel-wise analyses suffer if image registration is not done properly or lesion locations vary between subjects, and thus sensitivity is lost [7, 8].

A few recent studies [9, 10, 11] have proposed performing analyses along a defined ROI tract and creating its tract profile. This approach, called tract-based or along-tract analysis, has the ability to study large regions of interest while maintaining sensitivity to small and/or localized changes.

Colby[9], Yeatman[10], and Walsh[11] all extract the orientation of any defined ROI with the help of tractography. Tractography estimates the principal orientation direction of any white matter tract providing continuous streamlines through a three-dimensional brain volume [12, 13]. Different algorithms were used to perform tractography by these researchers. Colby et al. used Fiber Assignment by Continuous Tracking (FACT) [12] to obtain tractography and then resampled the obtained

streamlines using a cubic B-splines algorithm. Yeatman et al. performed tractography using deterministic streamline tracking algorithm (STT) [12, 13] and each streamline was equally resampled to include 100 nodes. Walsh et al. took the help of DTI studio to perform tractography using specific parameters [14]. Once the tractography is done, all the three above studies made tract profiles by performing cross-sectional analyses at each node on the resampled streamlines.

The results of these studies are promising; however, they have a few limitations, which are as follows:

1. These studies use platform-dependent software, which is exclusively for Linux-based systems.
2. They use complicated, in-house software that requires knowledge of text-based programming.
3. They are exclusively for DTI data where tractography is performed beforehand and thus, cannot be used for other white matter imaging modalities (such as T1w/T2w ratio, magnetization transfer imaging, multi-component T2-weighted myelin water imaging, etc.).

3.2 Objective

In this paper, the aim is ultimate to create a standalone novel toolbox – called “Quantitative Tract Integrity Profiles (Q-TIPs)”- to extract any white matter imaging metric along any volume, thereby allowing the integration of multiple measures of white matter integrity along individual regions of interest. Q-TIPs addresses the issues mentioned above of recent studies as follows.

1. This toolbox is purely MATLAB based. MATLAB is easily accessible and runs on most operating systems.
2. Graphical user interface (GUI) along with open-source code will be provided. GUIs make it easier to operate without having any knowledge of text-based programming. The open-source code allows anyone having knowledge of programming, to modify it according to his or her requirements.
3. Q-TIPS extracts the orientation of any ROI mask by calculating the medial axis using Voronoi and Delaunay algorithms (as discussed in the previous chapter). Analyses performed on the cross-sectional slicing made along the medial axis can create tract profiles. In this way, tract-based analyses can be done for any white matter imaging techniques.

All the image-processing steps are discussed in detail in the methodology section below.

3.3 Methodology

Any binary ROI mask and any quantitative image (such as a T1w/T2w ratio map – that are co-registered/aligned in the same coordinate space) are required as inputs for Q-TIPS. The Q-TIPS pipeline, starting from raw binary fiber to finally produce cross-sectional slicing, is shown in Figure 3-1. The algorithms used in each step are briefly described in the following sections.

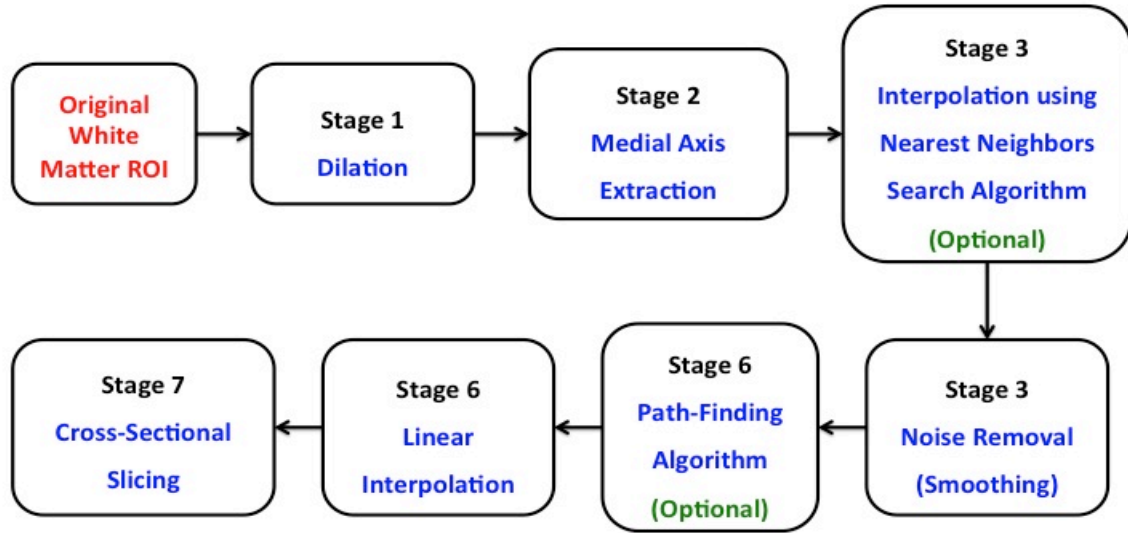


Figure 3-1: Image processing pipeline of Q-TIPs.

3.3.1 Dilation

Morphological dilation is an image processing technique that enlarges the binary object present in the image by adding additional pixels to its boundaries[15]. Structure elements are used during the dilation process to expand the object [16]. A structure element is also a binary mask that allows us to define arbitrary neighborhood structures [17]. During dilation, the object is expanded to reduce any discontinuities (i.e. gaps/holes in the white matter ROI mask). Dilation of an image with 3x3 structure element is shown in Figure 3-2.

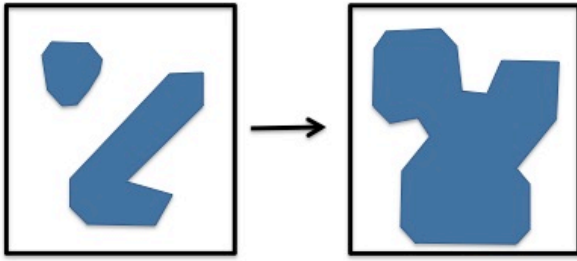


Figure 3-2: Effect of dilation using 3x3 structure element. It can see that gap between two objects can be reduced using dilation method.

Since white matter ROI masks may not be continuous, a smooth object with regular boundaries, they may have to be dilated and smoothed before the medial axis can be extracted. If required the dilation process is visually controlled by the operator, meaning that there is no algorithm to check how much dilation is necessary to smooth the fiber tract while maintaining the topology of that tract. Proper dilation results are shown in Figure 3-3.

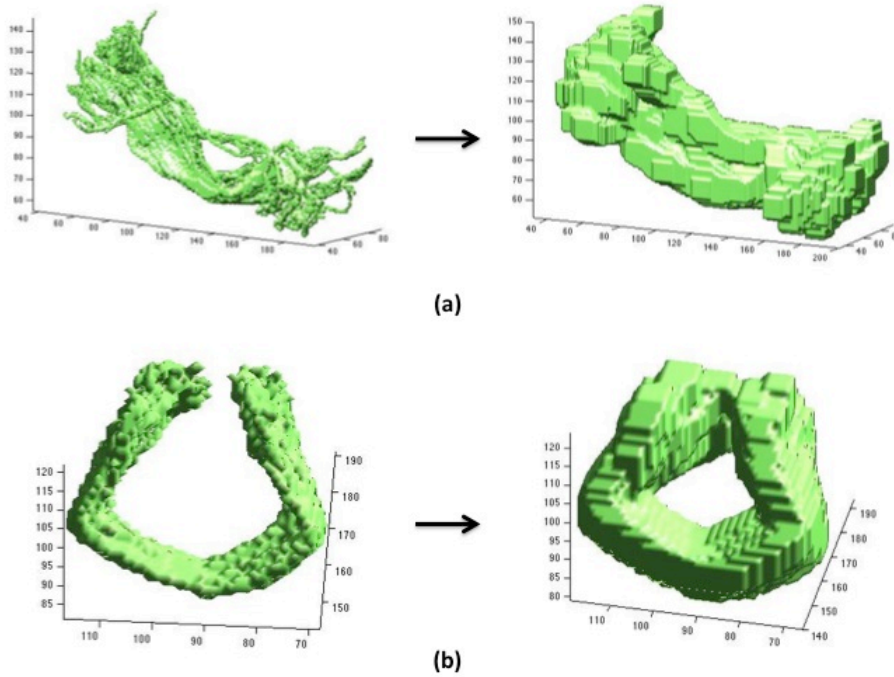


Figure 3-3: Dilation process in Q-TIPs. (a) Fiber tract is dilated five times using 3x3x3 cubic structure element. (b) Fiber tract is dilated three times using 3x3x3 cubic structure elements.

Too little dilation may make it difficult to extract the medial axis, as it might leave discontinuities within the tract; while on the other hand, too much dilation may ruin the topology of the white matter tract, resulting in a medial axis that does not accurately represent the original shape. Improper dilation results are shown in Figure 3-4.

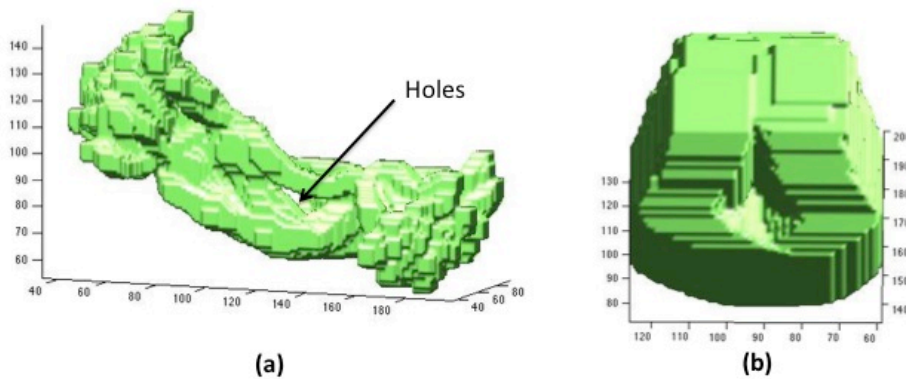


Figure 3-4: Improper dilation results (a) Fiber tract dilated three times using 3x3x3 cubic structure leaving holes within the tract. (b) Fiber tract dilated ten times using 3x3x3 cubic structure ruins the topology

3.3.2 Medial Axis Extraction

Once the white matter ROI mask is smooth and continuous (without gaps or holes), the medial axis is extracted using our previously described “divide and conquer” technique (see the previous chapter).

3.3.3 Noise Removal/Smoothing of Medial Axis

Although the extracted medial axis is continuous and one voxel thin, it is not smooth, and in fact, contains small offsets (zigzags). These offsets make it hard to perform cross-sectional slicing due to a high degree of variation in angle between adjacent points along the medial axis. This noise is removed by defining a neighborhood

and then replacing it by their average location as illustrated in Figure 3-5 [18]. Some of the information about the medial axis is also removed along with the noise, creating wide gaps in the medial axis. These deficiencies are again filled using simple linear interpolation.

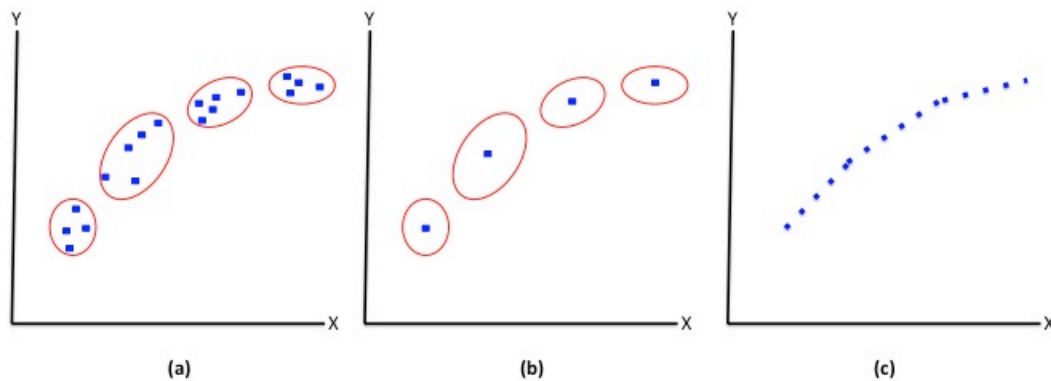


Figure 3-5: Noise Removal Algorithm. (a) Original extracted medial axis has too much variation. Points are grouped together according to defined neighborhood. (b) Grouped points are replaced by their average location. (c) Linear interpolation is performed to obtain missing information.

3.3.4 Path-Finding Algorithm

The path-finding algorithm is not necessary for a medial axis having two end points since (by definition) one of them will be a starting point, and the other will be the end point. For the medial axis with multiple ends, the path-finding algorithm is necessary if a researcher wants to perform analyses between two specific endpoints. There are many path-finding algorithms quoted in literature that can handle complex situations [19, 20, 21].

In Q-TIPs, the problem of path-finding is dealt with by labeling features of the medial axis. These features include branches, bifurcations, and lakes, as shown in Figure

3-6. Among these features, lakes are most the difficult to handle. These features are labeled first, and then their relationships on their neighborhood features are made as shown in Figure 3-7. This relationship list used to look for a particular path, e.g. if someone wants to perform analysis from point 1 to point 2. By searching through the relationship list, it can be found that the path between 1 & 2 includes key points (60, 5 and 70). Using these key points, the path is defined as (1→60→5→70→2). All the possible results of a path-finding algorithm on an example fiber tract are shown in Figure 3-8.

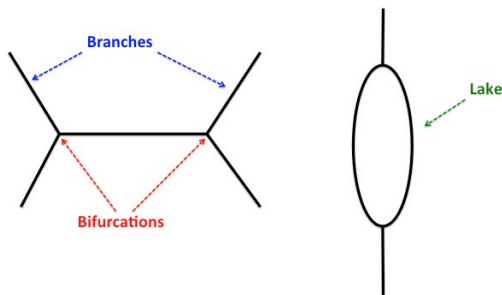


Figure 3-6: Complex features of medial axes.

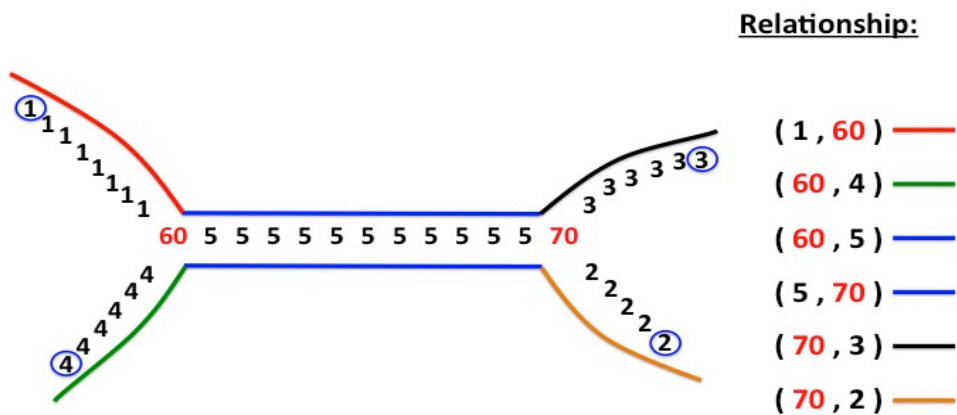


Figure 3-7: Feature labeling (branches and bifurcations). Blue circles are end points, and red numbers are bifurcation points. On the right, relationships are shown that describe each possible segment that could be combined to chart a path between any starting point and any end point.

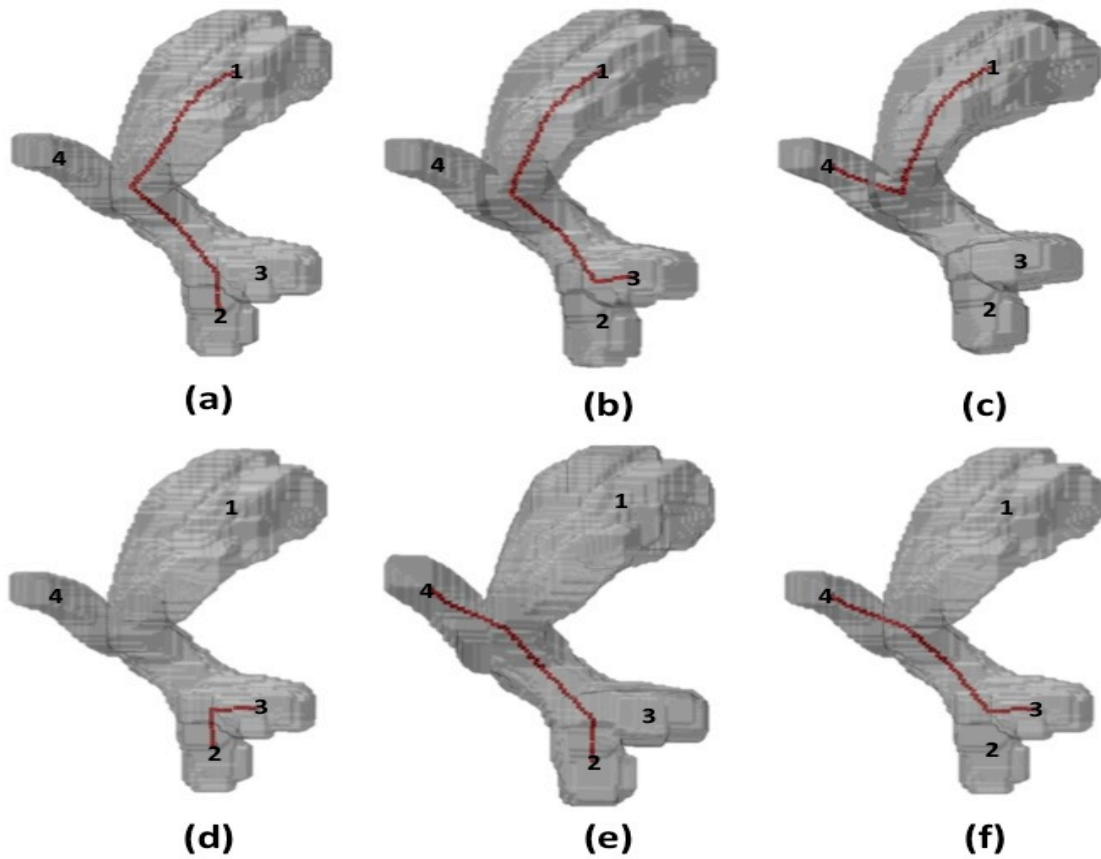


Figure 3-8: Results of path-finding algorithm. (a) Path (1 to 2). (b) Path (1 to 3). (c) Path (1 to 4). (d) Path (2 to 3) (e) Path (2 to 4) (f) Path (3 to 4).

3.3.5 Cross-Sectional Slicing

The last stage is to perform cross-sectional slicing along the extracted medial axis, allowing tract-based analyses along the fiber. Cross-sectional slicing is making slices perpendicular to the direction of the medial axis at particular points along the path. Figure 3-9 illustrates the cross-sectional slicing process at P_1 . P_1 and P_2 are two adjacent points along the medial axis and $\overrightarrow{P_1P_2}$ is a vector in the direction of the medial axis. Red filled circle is made at P_1 , which is perpendicular to $\overrightarrow{P_1P_2}$. The dot product of any radius vector

of that circle and the vector $\overrightarrow{P_1P_2}$ is zero. Two vector \vec{A} and \vec{B} are considered perpendicular when their dot product is zero ($\vec{A} \cdot \vec{B} = AB \cos \theta = 0$), where θ is the angle between vector \vec{A} and \vec{B} .

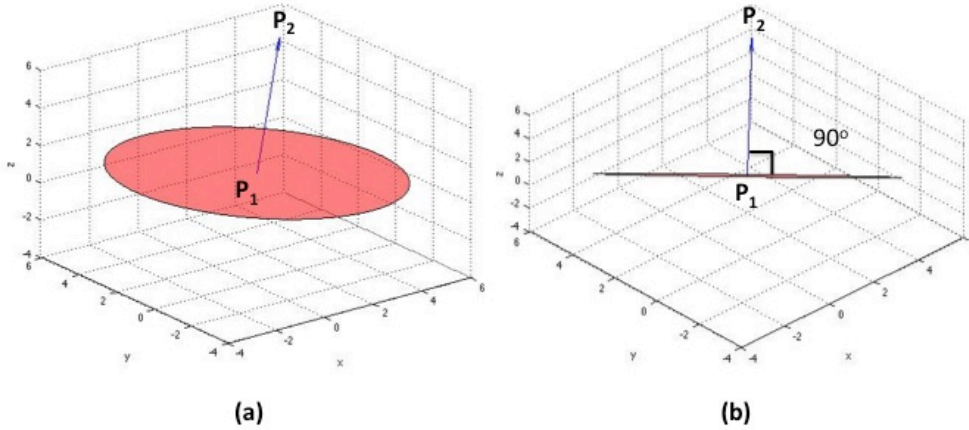


Figure 3-9: Perpendicular direction at P_1 .

After calculating the perpendicular direction, the size of the slice is determined by drawing multiple circles at that particular point. The radius of the circle is increased until the outer edge of the white matter ROI boundary is inside that circle. This largest radius (green circle in Figure 3-10) will provide the size of the slice that has to be made at that point. After slicing, the plane is then masked using the original (undilated) ROI mask so that only accurate coordinates within the original ROI are included.

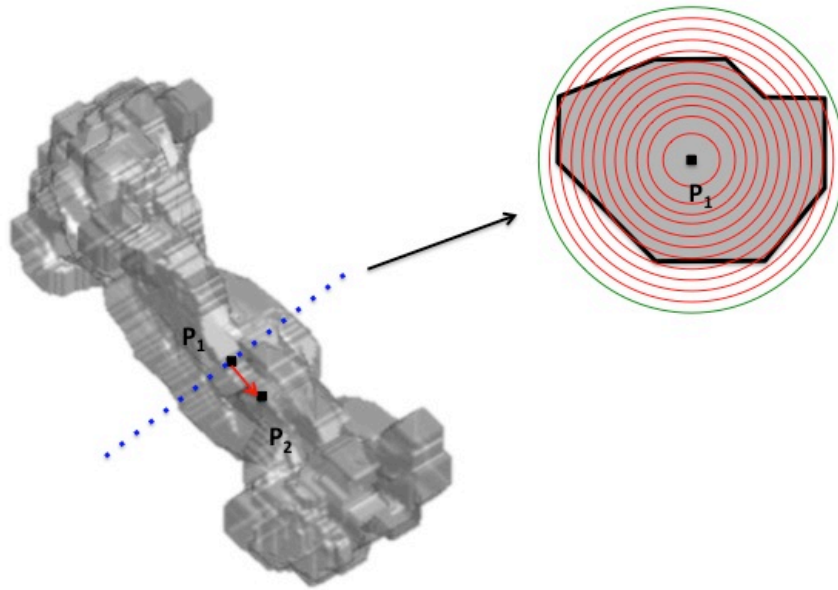


Figure 3-10: Slicing performed at P_1 and masking with the cross-section of the original (undilated) ROI.

3.4 Functional Flowchart for Q-TIPs

The functional flow chart of Q-TIPs is shown in Figure 3-11. A quantitative white matter map is one of the two inputs required for proper functioning of Q-TIPs. Using this map/atlas, it extracts the medial axis and makes the cross-sectional slices. Another input of Q-TIPs is any white matter imaging data. Values (e.g. T1w/T2w ratio, myelin water fraction, fractional anisotropy and mean diffusivity, etc.) from white matter imaging data are extracted using the information from the cross-sectional slices and finally, creates a tract profile.

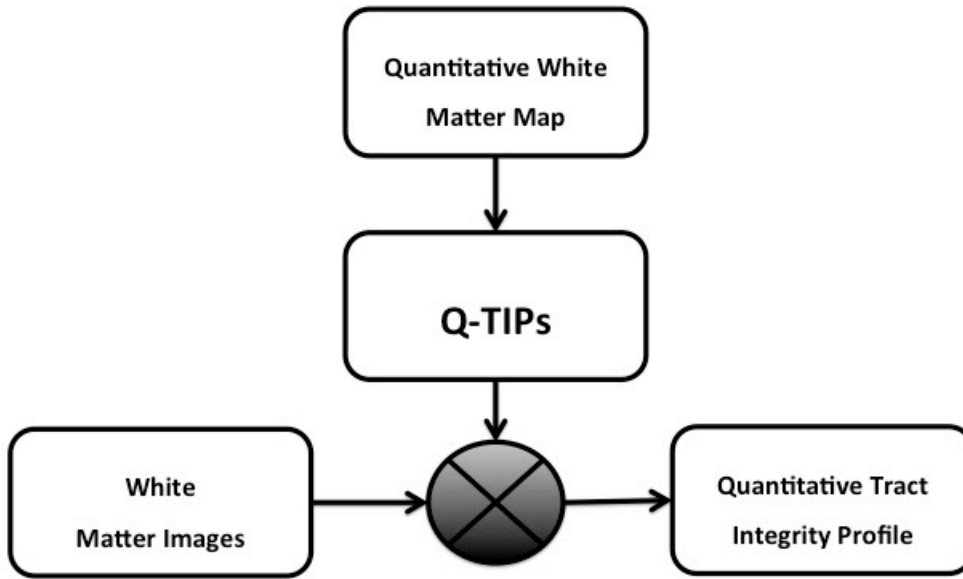


Figure 3-11: Functional flowchart of Q-TIPs.

3.5 Results

In this section, we chose a random assortment of fiber tracts from the UManitoba-JHU Functionally-Defined White Matter Atlas [22] to show outputs at different stages of the Q-TIPs pipeline. Figure 3-12 shows the results obtained for each Q-TIPs stage except for stage 3. Stage 3, interpolation using the nearest neighbors search algorithm, is not required because the medial axis extracted at stage 2 is continuous. Also, this fiber tract has only two points (either of which can be starting or ending points); therefore, the path-finding algorithm stage was also skipped.

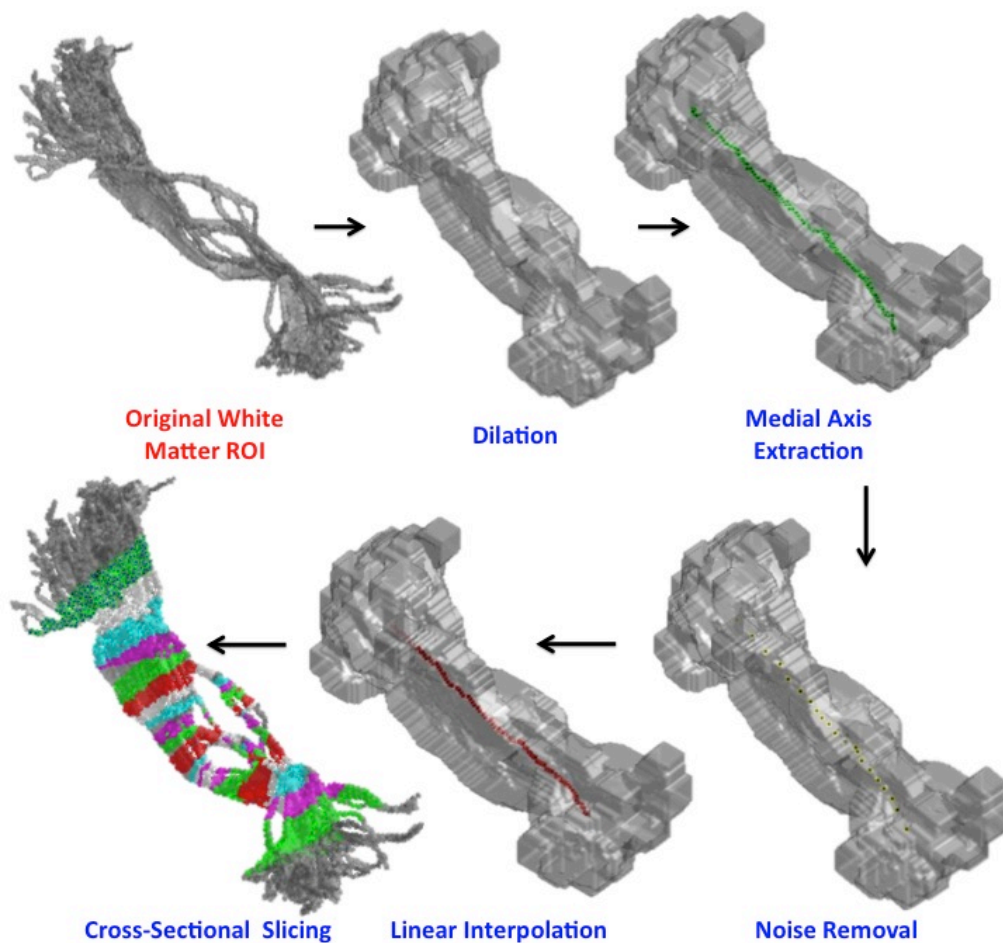


Figure 3-12: Outputs at different stages of Q-TIPs for a representative white matter ROI mask (from an existing atlas).

Figure 3-13 shows the results obtained for a more complex U-shaped white matter atlas. Here the interpolation using nearest neighbors search algorithm; stage 3 is done because the medial axis extracted at stage 2 contains gaps, and thus, intelligent interpolation is required after stage 2. However, the path-finding algorithm (stage 5) is skipped here because this fiber also has only two endpoints.

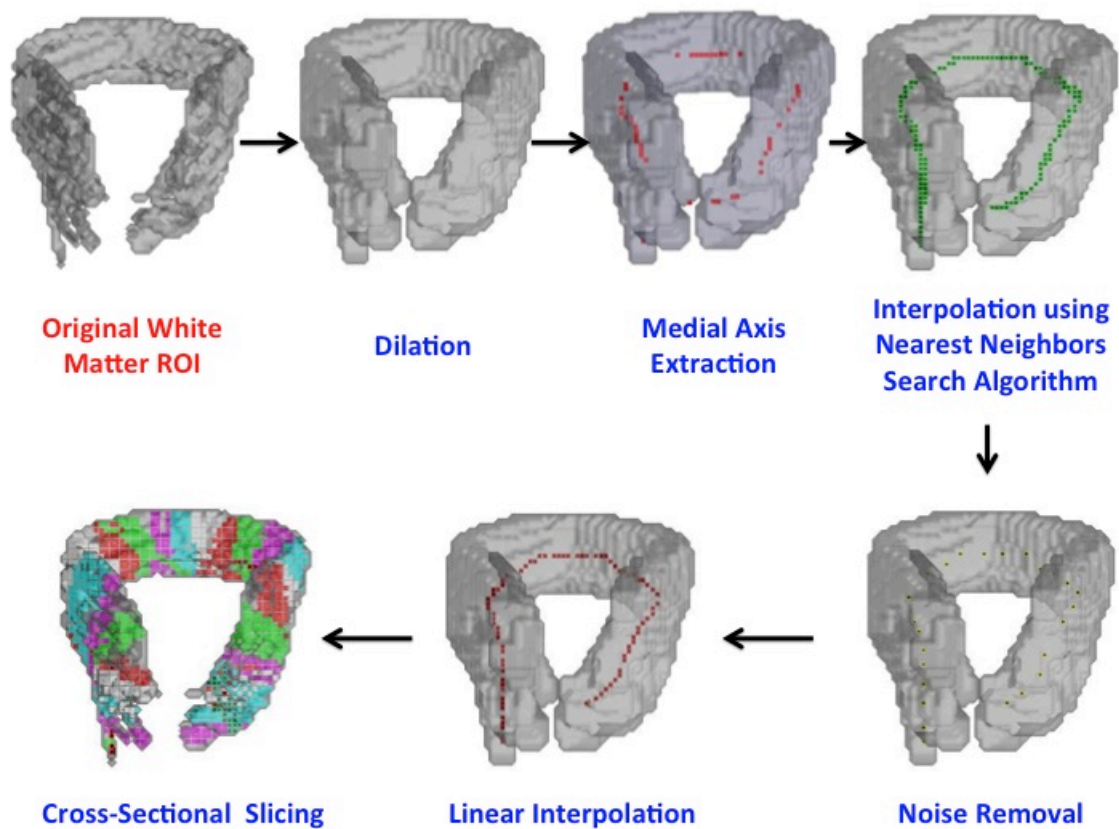


Figure 3-13: Outputs at different stages of Q-TIPs for a different white matter ROI mask (from an existing atlas).

Figure 3-14 shows the outputs of Q-TIPs for a third and much more complex white matter ROI. The fiber has multiple ending points. Therefore the path-finding algorithm is required, and the user must specify which two points s/he wants to perform along-tract analyses.

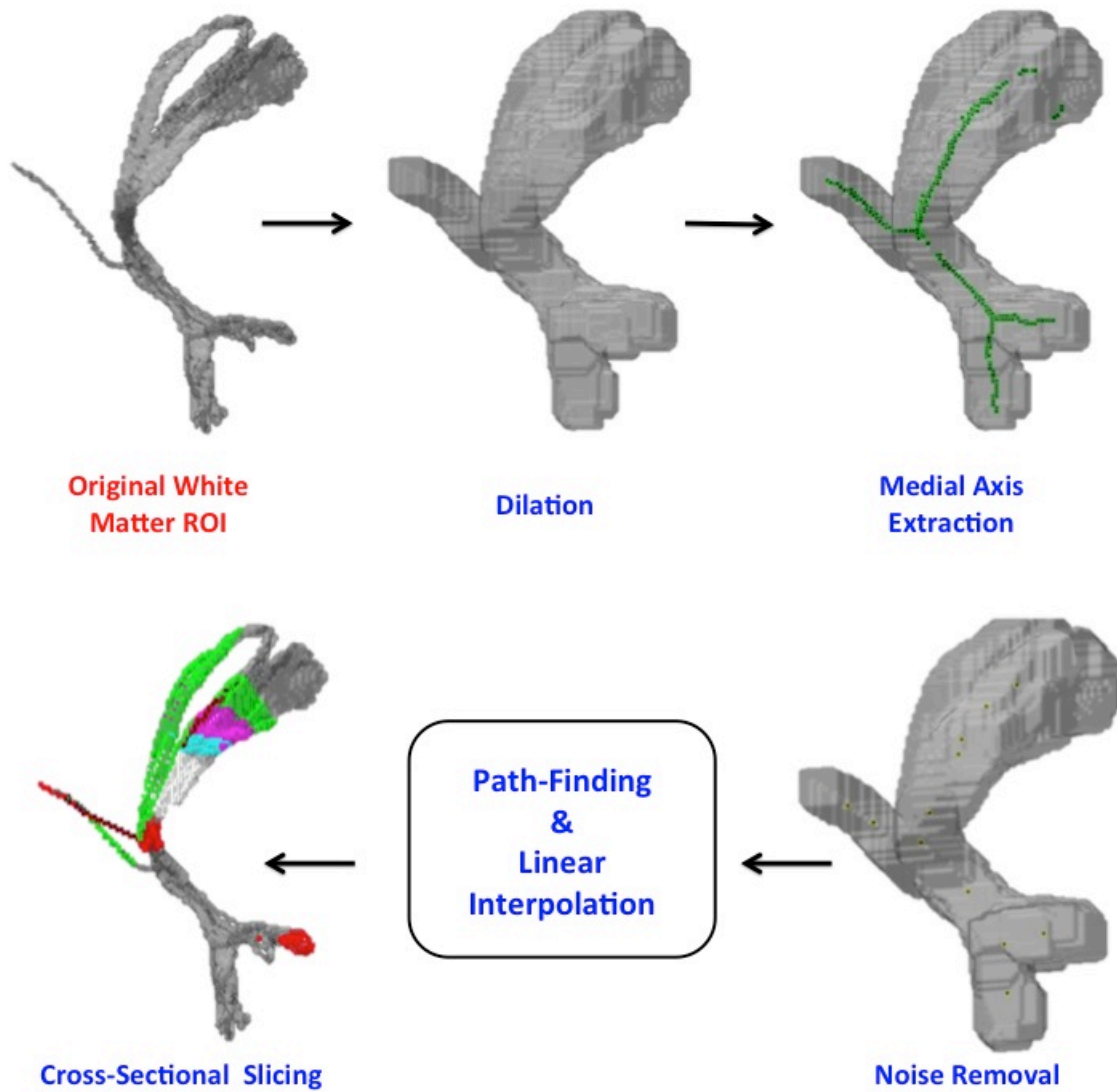


Figure 3-14: Outputs at different stages of Q-TIPs for a multi-ends white matter ROI mask (from an existing atlas).

Figure 3-15 shows the tract profiles generated using our toolbox Q-TIPs. In this experiment, the information of the cross-sectional slices (generated in Figure 3-12) is used to extract different average values (such as T1w/T2w ratio, FA, MD, and MWF) for a randomly selected subject from UManitoba-JHU Functionally-Defined White Matter data.

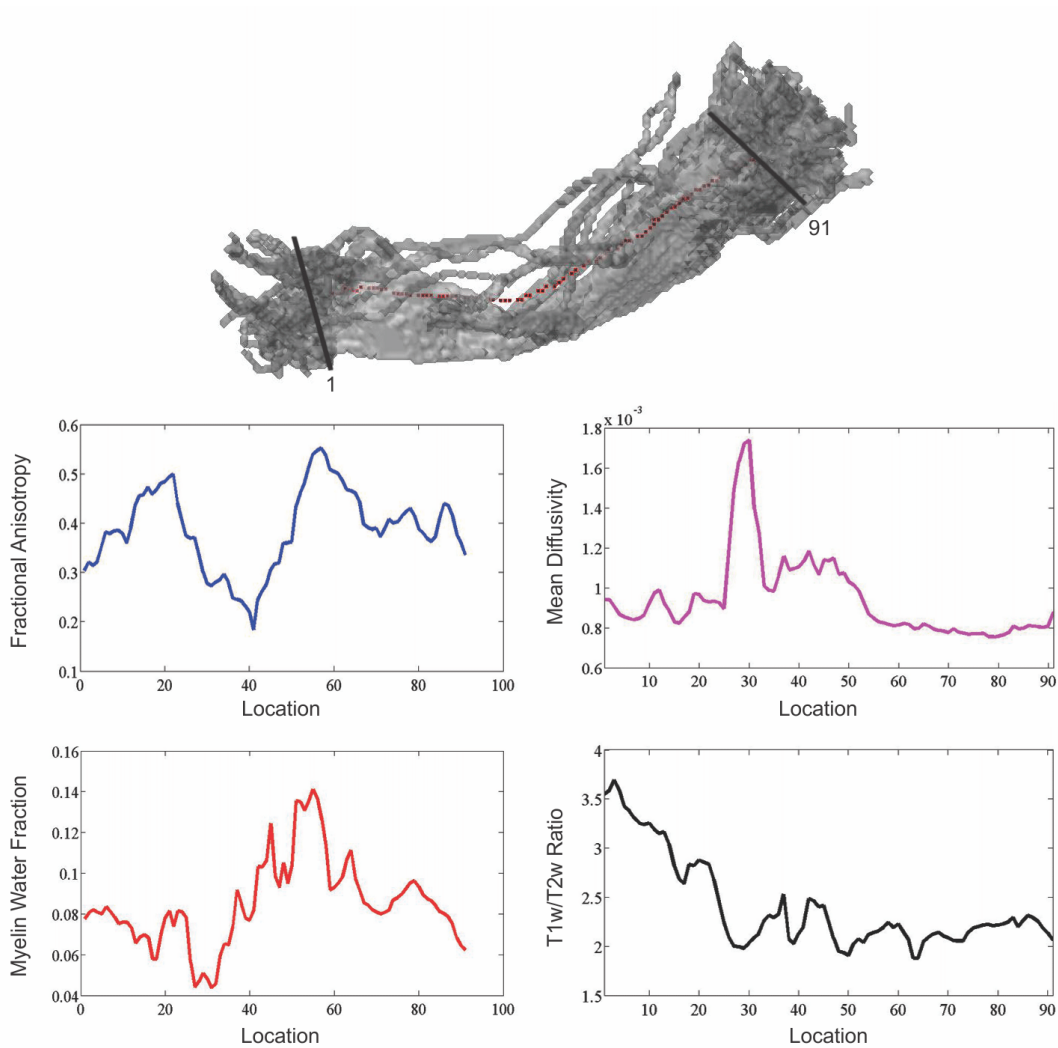


Figure 3-15: Tract-profiles (fractional anisotropy, mean diffusivity profile, myelin water fraction, and T1w/T2w ratio) are generated using Q-TIPs.

Figure 3-16 shows another set of tract profiles that are generated for the same subject using cross-sectional slices information extracted for another white matter atlas (see Figure 3-13).

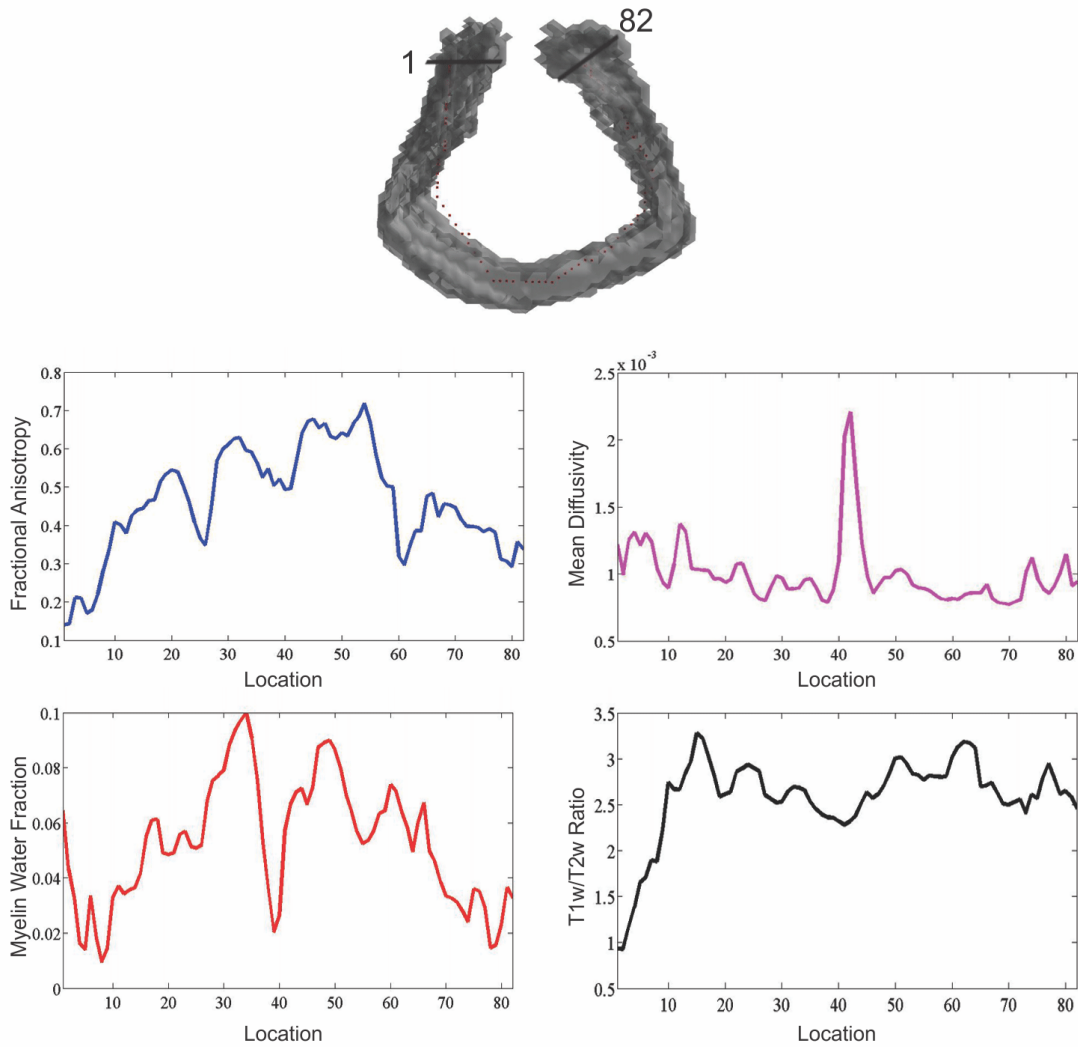


Figure 3-16: Tract-profiles (fractional anisotropy, mean diffusivity profile, myelin water fraction, and T1w/T2w ratio) are generated using Q-TIPs.

3.6 Discussion

Our results show that Q-TIPs efficiently performs tract-based analyses on complex white matter atlases without having the knowledge of tractography. Previous tract-based studies [9][10][11] require tractography to perform along-tract analyses, which limit their scope to only DTI data. Our toolbox “Q-TIPs” addresses this problem by extracting the medial axis of any given ROI and then reslicing the image orthogonally along the medial axis. In this way, it can be used to carry out similar analyses on non-diffusion based metrics (such as T1w/T2w ratio, magnetization transfer imaging, multi-component T2-weighted myelin water imaging, etc.), and can be used with any white matter atlas (e.g., JHU "Eve" atlas [23], the UManitoba-JHU Functionally-Defined White matter atlases [22], etc.).

However, despite the gains made in the current work, Q-TIPs still has a few remaining limitations, which can be addressed in future refinements of this toolbox.

- 1) Over-smoothing (too much dilation) of the white matter atlas may lose information while under smoothing (less dilation) may result in an inaccurate medial axis. Therefore, while the user must manually set the correct amount of smoothing for each mask in the current software version, future versions could employ an automatic adaptive smoothing algorithm to maintain the topology of the white matter atlases.
- 2) In the path-finding algorithm, lakes (one of the difficult features) will need to be more thoroughly addressed in future developments of this toolbox. For now, Q-TIPs will crash if there are lakes in the extracted medial axis.

3) In white matter ROIs with sharp bends, incorrect cross-sectional slicing (red color in Figure 3-17) sometimes happens. This occurs because the noise removal algorithm also eliminates some medial axis information along with the noise. Therefore, when these gaps are filled using simple linear interpolation, the bending information of the tract is lost.

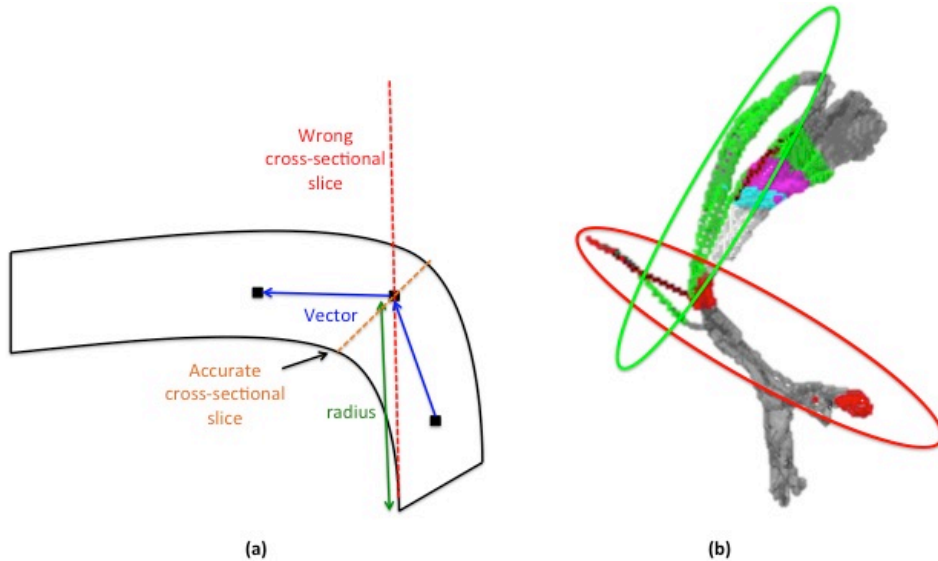


Figure 3-17: Example of the wrong cross-sectional slice at bends. (b) Red and green circles indicate results of wrong cross-sectional slicing.

3.7 Conclusion

In this paper, we have developed a novel “Quantitative Tract Integrity Profiles (Q-TIPs)” toolbox for assessing the integrity of white matter tracts using along-tract analysis. Q-TIPs addresses several of the limitations that exist in previously reported tract-based analysis studies [9][10][11]. Q-TIPs is a standalone toolbox, independent of platform and is compatible with any white matter imaging modality. Results show that Q-TIPs extract the cross-sectional slices using the orientation of extracted medial axis of

any ROI atlas. This toolbox will facilitate the investigation of structure-function and structure-behavior correlations among patients with various white matter disorders and is therefore expected to have a broad range of research and clinical applications.

3.8 References

- [1] A. Nieto-Castanon, S. S. Ghosh, J. A. Tourville, and F. H. Guenther, “Region of interest based analysis of functional imaging data,” *Neuroimage*, vol. 19, no. 4, pp. 1303–1316, 2003.
- [2] R. A. Poldrack, “Region of interest analysis for fMRI,” *Soc. Cogn. Affect. Neurosci.*, vol. 2, no. 1, pp. 67–70, 2007.
- [3] D. H. Salat, D. S. Tuch, D. N. Greve, A. J. W. Van Der Kouwe, N. D. Hevelone, A. K. Zaleta, B. R. Rosen, B. Fischl, S. Corkin, H. Diana Rosas, and A. M. Dale, “Age-related alterations in white matter microstructure measured by diffusion tensor imaging,” *Neurobiol. Aging*, vol. 26, no. 8, pp. 1215–1227, 2005.
- [4] M. Ota, T. Obata, Y. Akine, H. Ito, H. Ikehira, T. Asada, and T. Suhara, “Age-related degeneration of corpus callosum measured with diffusion tensor imaging,” *Neuroimage*, vol. 31, no. 4, pp. 1445–1452, 2006.
- [5] S. M. Smith, M. Jenkinson, H. Johansen-Berg, D. Rueckert, T. E. Nichols, C. E. Mackay, K. E. Watkins, O. Ciccarelli, M. Z. Cader, P. M. Matthews, and T. E. J. Behrens, “Tract-based spatial statistics: Voxelwise analysis of multi-subject diffusion data,” *Neuroimage*, vol. 31, no. 4, pp. 1487–1505, 2006.

- [6] J. Ashburner and K. J. Friston, “Voxel-Based Morphometry—The Methods,” *Neuroimage*, vol. 11, no. 6, pp. 805–821, 2000.
- [7] X. Geng, G. E. Christensen, H. Gu, T. J. Ross, and Y. Yang, “Implicit reference-based group-wise image registration and its application to structural and functional MRI,” *Neuroimage*, vol. 47, no. 4, pp. 1341–1351, 2009.
- [8] J. Ashburner, “A fast diffeomorphic image registration algorithm,” *Neuroimage*, vol. 38, no. 1, pp. 95–113, 2007.
- [9] J. B. Colby, L. Soderberg, C. Lebel, I. D. Dinov, P. M. Thompson, and E. R. Sowell, “Along-tract statistics allow for enhanced tractography analysis,” *Neuroimage*, vol. 59, no. 4, pp. 3227–3242, 2012.
- [10] J. D. Yeatman, R. F. Dougherty, E. Rykhlevskaia, A. J. Sherbondy, G. K. Deutsch, B. A. Wandell, and M. Ben-Shachar, “Anatomical properties of the arcuate fasciculus predict phonological and reading skills in children,” *J. Cogn. Neurosci.*, vol. 23, no. 11, pp. 3304–17, 2011.
- [11] M. Walsh, C. A. Montojo, Y.-S. Sheu, S. A. Marchette, D. M. Harrison, S. D. Newsome, F. Zhou, A. L. Shelton, and S. M. Courtney, “Object working memory performance depends on microstructure of the frontal-occipital fasciculus,” *Brain Connect.*, vol. 1, no. 4, pp. 317–29, 2011.
- [12] S. Mori, B. J. Crain, V. P. Chacko, and P. C. M. van Zijl, “Three-dimensional tracking of axonal projections in the brain by magnetic resonance imaging,” *Ann. Neurol.*, vol. 45, no. 2, pp. 265–269, 1999.
- [13] P. J. Basser, S. Pajevic, C. Pierpaoli, J. Duda, and A. Aldroubi, “In vivo fiber tractography using DT-MRI data,” *Magn. Reson. Med.*, vol. 44, no. 4, pp. 625–

632, 2000.

- [14] H. Jiang, P. C. M. Van Zijl, J. Kim, G. D. Pearlson, and S. Mori, “DtiStudio: Resource program for diffusion tensor computation and fiber bundle tracking,” *Comput. Methods Programs Biomed.*, vol. 81, no. 2, pp. 106–116, 2006.
- [15] R. Gonzalez and R. Woods, *Digital image processing*. 2002.
- [16] O. Sigmund, “Morphology-based black and white filters for topology optimization,” *Struct. Multidiscip. Optim.*, vol. 33, no. 4–5, pp. 401–424, 2007.
- [17] C. Di Ruberto, A. Dempster, S. Khan, and B. Jarra, “Analysis of infected blood cell images using morphological operators,” *Image Vis. Comput.*, vol. 20, no. 2, pp. 133–146, 2002.
- [18] L. Ertöz, M. Steinbach, and V. Kumar, “Finding Clusters of Different Sizes, Shapes, and Densities in Noisy, High Dimensional Data,” *Proc. Second SIAM Int. Conf. Data Min.*, pp. 47–59, 2003.
- [19] I. Pohl, “Heuristic search viewed as path finding in a graph,” *Artif. Intell.*, vol. 1, no. 3–4, pp. 193–204, 1970.
- [20] A. Botea, M. Müller, and J. Schaeffer, “Near optimal hierarchical path-finding,” *J. game Dev.*, no. January 2004, pp. 1–30, 2004.
- [21] C. Y. Lee, “An Algorithm for Path Connections and Its Applications,” *Electron. Comput. IRE Trans.*, vol. EC-10, no. 3, pp. 1389–1401, 1961.
- [22] T. D. Figley, N. Bhullar, S. M. Courtney, and C. R. Figley, “Probabilistic atlases of default mode, executive control, and salience network white matter tracts: an fMRI-guided diffusion tensor imaging and tractography study,” *Front. Hum. Neurosci.*, vol. 9, no. November, p. Article 585, 2015.

- [23] K. Oishi, A. Faria, H. Jiang, X. Li, K. Akhter, J. Zhang, J. T. Hsu, M. I. Miller, P. C. M. van Zijl, M. Albert, C. G. Lyketsos, R. Woods, A. W. Toga, G. B. Pike, P. Rosa-Neto, A. Evans, J. Mazziotta, and S. Mori, “Atlas-based whole brain white matter analysis using large deformation diffeomorphic metric mapping: Application to normal elderly and Alzheimer’s disease participants,” *Neuroimage*, vol. 46, no. 2, pp. 486–499, 2009.

Chapter 4

General Discussion and Conclusion

In summary, this thesis describes the methods underlying our new “Quantitative Tract Integrity Profiles (Q-TIPs)” Toolbox for assessing the integrity along any white matter ROI. Previous quantitative white matter imaging approaches (i.e., ROI and voxel-wise analyses) have been reviewed along with their pros and cons. In addition, a few recently published tract-based analysis approaches are also mentioned, in which tract profiles are made along the defined ROIs with the help of tractography. Because of this, these tract-based analysis methods are restricted to the DTI data because they need streamlines (obtained during tractography) in order to move along the particular tract and thus, cannot easily be applied to other white matter imaging modalities (such as MTI, MWI, etc.).

To address this limitation, Q-TIPs extracts the medial axis of any given ROI mask or atlas and then performs cross-sectional slicing along the extracted medial axis. The medial axis is extracted using the general concept of ‘divide and conquer’ in which any 3D volume/image is split into multiple 2D images, and then, the Voronoi diagram is applied to each 2D image separately. The extracted 2D medial axes are again stacked in

their respective direction (the X-, Y- and Z-direction medial axes). An intersection approach is then used to find the common skeleton between any two directions (XY-, YZ-, ZX-common), as well as the intersections between all three directions (XYZ-common). Finally, the one that most accurately represents the skeleton of the original atlas is visually selected.

For complex fiber tracts, the outputs of the Voronoi algorithm sometimes contain discontinuities, plus the extracted medial axis points are not in sequence. Therefore, an intelligent interpolation algorithm is required to fill these gaps. Q-TIPs also proposes a novel “Nearest Neighbors Search Algorithm” using Delaunay triangles. Results show that our medial axis extraction pipeline efficiently extracts the skeletons of complex objects. Our proposed medial axis extraction algorithm is not only limited for white matter atlases but could also have applications in other image processing fields (such as video games, gait movement analyses, efficient data transfer, etc.).

After extracting the medial axis, cross-sectional slices can then be made along the white matter ROI, and tract profiles can be created without using tractography. The complete image-processing pipeline of Q-TIPs is also shown. Using our novel toolbox “Q-TIPs,” tract-based analyses can now be performed in any white matter ROI and for any white matter imaging technique.

4.1 Future Developments

Future developments related to Q-TIPs include:

4.1.1 Graphical User Interface (GUI)

A graphical user interface makes it easier to run the toolbox compared to a text-based, command-line interface. Therefore, in the future, a GUI with a flexible and user-friendly interface will be developed for Q-TIPs.

4.1.2 Optimizing Processing Time

Although we have shown that our software is able to analyze data in acceptable time-frames compared to other neuroimaging analyses (and is much faster than previous along-tract methods requiring tractography analysis), improvements could be made to make it even faster. Because Q-TIPs is purely based on MATLAB, the overall processing time could be reduced by performing matrix operations instead of loop operations. Beside this, multi-core CPUs (which are now standard) could be used more efficiently by leveraging MATLAB's parallel computing capabilities to process different operations in parallel on different cores of the processor.

4.1.3 Validation and Quantification of Tract Profiles

To validate our toolbox, diffusion tensor imaging (DTI), magnetization transfer imaging (MTI) and multi-component T2 myelin water imaging (MWI) on post-mortem human autopsy brains from MS patients, as well as age- and gender-matched neurologically healthy control subjects will be performed. White matter tracts will be defined based on anatomical atlases, and quantitative data (such as DTI, MTI, and MWI, etc.) will be extracted along the tract to make quantitative curves representing each white matter integrity measured as a function of location along the tract.

Curve fitting methods will be applied to assess whether patient groups exhibit decreased white matter integrity anywhere along each tract (i.e., curve), compared to the healthy control subjects. This will help to get some insight whether these changes are due to global (e.g. an average of the tract) or local (e.g. maximum deviation) changes or even both along the tract.

4.1.4 Releasing the Toolbox

Finally, once the remaining issues have been resolved and the toolbox has been validated, it will be freely distributed as a standalone toolbox for the popular Statistical Parametric Mapping (SPM) package.

Appendix A

List of Acronyms

A/D	Analogue-to-Digital
AFQ	Automated Fiber Quantification
BOLD	Blood Oxygenation Level–Dependent
CNS	Central Nervous System
CT	Computed Tomography
DARTEL	Diffeomorphic Anatomical Registration using Exponentiated Lie Algebra
DT	Distance Transforms
DTI	Diffusion Tensor Imaging
FA	Fractional Anisotropy
FACT	Fiber Assignment by Continuous Tracking
GUI	Graphical User Interface
HAMMER	Hierarchical Attribute Matching Mechanism for Elastic Registration
MAT	Medial Axis Transform
MD	Mean Diffusivity
MRI	Magnetic Resonance Imaging
MS	Multiple Sclerosis
MTI	Magnetization Transfer Imaging
MTR	Magnetization Transfer Ratio
MWF	Myelin Water Fraction

MWI	Myelin Water Imaging
NMR	Nuclear Magnetic Resonance
PET	Positron Emission Tomography
Q-TIPs	Quantitative Tract Integrity Profiles
RF	Radio Frequency
ROI	Region-of-Interest
SPM	Statistical Parametric Mapping
STT	Streamlines Tracking Algorithm
TBSS	Tract-Based Spatial Statistics

Appendix B

12/23/2016

RightsLink Printable License

ELSEVIER LICENSE TERMS AND CONDITIONS

Dec 23, 2016

This Agreement between Sohail Younas ("You") and Elsevier ("Elsevier") consists of your license details and the terms and conditions provided by Elsevier and Copyright Clearance Center.

License Number	4014890712271
License date	Dec 23, 2016
Licensed Content Publisher	Elsevier
Licensed Content Publication	NeuroImage
Licensed Content Title	Age-related degeneration of corpus callosum measured with diffusion tensor imaging
Licensed Content Author	Miho Ota, Takayuki Obata, Yoshihide Akine, Hiroshi Ito, Hiroo Ikehira, Takashi Asada, Tetsuya Suhara
Licensed Content Date	15 July 2006
Licensed Content Volume Number	31
Licensed Content Issue Number	4
Licensed Content Pages	8
Start Page	1445
End Page	1452
Type of Use	reuse in a thesis/dissertation
Intended publisher of new work	other
Portion	figures/tables/illustrations
Number of figures/tables/illustrations	3
Format	both print and electronic
Are you the author of this Elsevier article?	No
Will you be translating?	No
Order reference number	
Original figure numbers	3
Title of your thesis/dissertation	Quantitative Tract Integrity Profiles (Q-TIPs) A Novel Toolbox for Assessing Tract-Based White Matter Integrity
Expected completion date	Jan 2017
Estimated size (number of pages)	80
Elsevier VAT number	GB 494 6272 12

**ELSEVIER LICENSE
TERMS AND CONDITIONS**

Jan 30, 2017

This Agreement between Sohail Younas ("You") and Elsevier ("Elsevier") consists of your license details and the terms and conditions provided by Elsevier and Copyright Clearance Center.

License Number	4038931506193
License date	Jan 30, 2017
Licensed Content Publisher	Elsevier
Licensed Content Publication	NeuroImage
Licensed Content Title	Tract-based spatial statistics: Voxelwise analysis of multi-subject diffusion data
Licensed Content Author	Stephen M. Smith, Mark Jenkinson, Heidi Johansen-Berg, Daniel Rueckert, Thomas E. Nichols, Clare E. Mackay, Kate E. Watkins, Olga Ciccarelli, M. Zaheer Cader, Paul M. Matthews, Timothy E.J. Behrens
Licensed Content Date	15 July 2006
Licensed Content Volume Number	31
Licensed Content Issue Number	4
Licensed Content Pages	19
Start Page	1487
End Page	1505
Type of Use	reuse in a thesis/dissertation
Intended publisher of new work	other
Portion	figures/tables/illustrations
Number of figures/tables/illustrations	1
Format	both print and electronic
Are you the author of this Elsevier article?	No
Will you be translating?	No
Order reference number	
Original figure numbers	17
Title of your thesis/dissertation	Quantitative Tract Integrity Profiles (Q-TIPs) A Novel Toolbox for Assessing Tract-Based White Matter Integrity
Expected completion date	Jan 2017
Estimated size (number of pages)	80
Elsevier VAT number	GB 494 6272 12

Licenses and Copyright

The following policy applies to all PLOS journals, unless otherwise noted.

What Can Others Do with My Original Article Content?

PLOS applies the Creative Commons Attribution (CC BY) license to articles and other works we publish. If you submit your paper for publication by PLOS, you agree to have the CC BY license applied to your work. Under this Open Access license, you as the author agree that anyone can reuse your article in whole or part for any purpose, for free, even for commercial purposes. Anyone may copy, distribute, or reuse the content as long as the author and original source are properly cited. This facilitates freedom in re-use and also ensures that PLOS content can be mined without barriers for the needs of research.

May I Use Content Owned by Someone Else in My Article?

If you have written permission to do so, yes. If your manuscript contains content such as photos, images, figures, tables, audio files, videos, etc., that you or your co-authors do not own, we will require you to provide us with proof that the owner of that content (a) has given you written permission to use it, and (b) has approved of the CC BY license being applied to their content. We provide a form you can use to ask for and obtain permission from the owner. Download the form (PDF).

i If you do not have owner permission, we will ask you to remove that content and/or replace it with other content that you own or have such permission to use.

Don't assume that you can use any content you find on the Internet, or that the content is fair game just because it isn't clear who the owner is or what license applies. It's up to you to ascertain what rights you have—if any—to use that content.

May I Use Article Content I Previously Published in Another Journal?

Many authors assume that if they previously published a paper through another publisher, they own the rights to that content and they can freely use that content in their PLOS paper, but that's not necessarily the case – it depends on the license that covers the other paper. Some publishers allow free and unrestricted re-use of article content they own, such as under the CC BY license. Other publishers use licenses that allow re-use only if the same license is applied by the person or publisher re-using the content.

If the paper was published under a CC BY license or another license that allows free and unrestricted use, you may use the content in your PLOS paper provided that you give proper attribution, as explained above.

If the content was published under a more restrictive license, you must ascertain what rights you have under that license. At a minimum, review the license to make sure you can use the content. Contact that publisher if you have any questions about the license terms – PLOS staff cannot give you legal advice about your rights to use third-party content. If the license does not permit you to use the content in a paper that will be covered by an unrestricted license, you must obtain written permission from the publisher to use the content in your PLOS paper. Please do not include any content in your PLOS paper which you do not have rights to use, and always give proper attribution.

What Are Acceptable Licenses for Data Repositories?

If any relevant accompanying data is submitted to repositories with stated licensing policies, the policies should not be more restrictive than CC BY.

Removal of Content Used Without Clear Rights

PLOS reserves the right to remove any photos, captures, images, figures, tables, illustrations, audio and video files, and the like, from any paper, whether before or after publication, if we have reason to believe that the content was included in your paper without permission from the owner of the content.

**ELSEVIER LICENSE
TERMS AND CONDITIONS**

Dec 23, 2016

This Agreement between Sohail Younas ("You") and Elsevier ("Elsevier") consists of your license details and the terms and conditions provided by Elsevier and Copyright Clearance Center.

License Number	4014890010135
License date	Dec 23, 2016
Licensed Content Publisher	Elsevier
Licensed Content Publication	NeuroImage
Licensed Content Title	Along-tract statistics allow for enhanced tractography analysis
Licensed Content Author	John B. Colby,Lindsay Soderberg,Catherine Lebel,Ivo D. Dinov,Paul M. Thompson,Elizabeth R. Sowell
Licensed Content Date	15 February 2012
Licensed Content Volume Number	59
Licensed Content Issue Number	4
Licensed Content Pages	16
Start Page	3227
End Page	3242
Type of Use	reuse in a thesis/dissertation
Portion	figures/tables/illustrations
Number of figures/tables/illustrations	3
Format	both print and electronic
Are you the author of this Elsevier article?	No
Will you be translating?	No
Order reference number	
Original figure numbers	3
Title of your thesis/dissertation	Quantitative Tract Integrity Profiles (Q-TIPs) A Novel Toolbox for Assessing Tract-Based White Matter Integrity
Expected completion date	Jan 2017
Estimated size (number of pages)	80
Elsevier VAT number	GB 494 6272 12



JOHNS HOPKINS
KRIEGER SCHOOL
of ARTS & SCIENCES

**DEPARTMENT OF PSYCHOLOGICAL
AND BRAIN SCIENCES**
3400 N. Charles Street, Ames Hall 232
Baltimore, Maryland 21218-2686
(p) 410.516.8894 / (f) 410.516.4478

February 1, 2017

Good afternoon Mr. Younas:

As the corresponding author, you have my permission to reproduce Figure 4 from our paper (details below) in the general introduction to your thesis, as long as our work is given proper credit.

In this regard, please clearly reference our paper somewhere in your figure caption, and make sure that the complete citation details are included in your References/Bibliography section.

Megan Walsh, Caroline A. Montojo, Yi-Shin Sheu, Steven A. Marchette, Daniel M. Harrison, Scott D. Newsome, Feng Zhou, Amy L. Shelton, and Susan M. Courtney. *Brain Connectivity*. October 2011, 1(4): 317-329.
doi:10.1089/brain.2011.0037.
Sincerely,

Susan Courtney, Ph.D.
Professor and Chair